Effects of stochastic generation on the elastic and inelastic spectra of fully non-stationary accelerograms

Probabilistic Engineering Mechanics 71 (2023) 103377

Contents lists available at ScienceDirect

Probabilistic Engineering Mechanics

journal homepage: www.elsevier.com/locate/probengmech

Effects of stochastic generation on the elastic and inelastic spectra of fully non-stationary accelerograms

Federica Genovese [a,b,c], Giuseppe Muscolino [a], Alessandro Palmeri [b,d,*]

[a] Università degli Studi di Messina, Messina, 98158, Italy
[b] Loughborough University, Loughborough, LE11 3TU, UK
[c] Università degli Studi Mediterranea di Reggio Calabria, Reggio Calabria, 89124, Italy
[d] Politecnico di Torino, Turin, 10129, Italy

ARTICLE INFO

Keywords:
Artificial accelerogram
Ground motion record
Earthquake engineering
Evolutionary power-spectral density
Inelastic response spectrum
Non-stationary stochastic process
Signal processing
Wavelet transform

ABSTRACT

Nonlinear dynamic analyses are a state-of-the-art tool to assess the performance of earthquake-resistant structures. Inevitably, the validity of the predicted seismic response depends on the fidelity of the computational model to the actual structural behavior and the representativeness of the time histories of ground acceleration as realizations of the seismic hazard for the site under consideration. The generation of artificial time histories is generally allowed by international seismic codes and represents a valid alternative to recorded accelerograms, provided that the key features in the expected seismic input are preserved in the generated signals. Different stochastic generation methods of fully non-stationary accelerograms have been proposed in the literature. Two alternative randomization strategies are compared in this paper, based on (*i*) wavelets analysis and (*ii*) evolutionary power spectral density (PSD) functions. The analyses are focused on the aleatory variability observed in the generated elastic and inelastic response spectra in relation to different modeling choices, offering qualitative and quantitative information to designers using stochastically generated accelerograms.

1. Introduction

The definition of the seismic action plays a fundamental role in the analysis of earthquake-resistant structures, especially if they are designed to exceed the linear-elastic range when exposed to severe ground motions. Typically, earthquake engineering codes provide the elastic and inelastic response spectra to quantify the seismic action for various return periods, importance classes and soil conditions (e.g., [1]). While the elastic spectra at the "damage limitation requirement" (DLR) depend on the equivalent viscous damping ratio, inelastic spectra at the "no-collapse requirement" (NCR) are derived for a chosen value of the ductility demand (or, alternatively, the "behavior" or "reduction" factor).

Response spectrum analyses are widely recognized as the reference method for the seismic design of conventional structures (e.g., [2]). However, time-history analyses are often preferable to better understand and quantify the nonlinear behavior of structures under seismic events of increasing intensity, especially in the case of non-conventional architectural forms and lateral-resisting systems. When performing nonlinear seismic analyses, the selection of a representative set of accelerograms is a crucial issue as it is influenced by multiple sources of uncertainties related to the definition of the seismic hazard (e.g., [3]). Generally, the selection is based on three different types of time histories, namely: (*i*) linearly scaled accelerograms recorded on sites with similar soil conditions; (*ii*) artificial or synthetic signals, "compatible" with a target response spectrum, e.g., using a "uniform hazard spectrum"; (*iii*) artificial accelerograms generated from a "parent signal" that is deemed to be representative of the seismic hazard at the site of interest.

The increasing availability of strong-motion records makes linearly scaled records an attractive option for defining the seismic excitation in several design situations. Different procedures for selecting proper sets of recorded accelerograms are available in the literature (e.g., [4]). However, there are cases in which it is not possible to obtain the minimum number of accelerograms required by the seismic codes without applying large scale factors to each record, which in turn may distort the salient characteristics of the recorded accelerogram. It has been shown (e.g., [5–10]) that the bias introduced by the scaling depends on the type of structure and type of seismic performance under investigation.

The use of spectrum-compatible artificial accelerograms instead of linearly scaled recorded ground motions is particularly appealing in many regions of the world where recorded accelerograms are scarce [11]. Starting from the pioneering work by Vanmarcke and Gasparini [12], several methods have been proposed to generate stationary, spectrum-compatible Gaussian processes [13–21]. However, artificial

* Corresponding author at: Loughborough University, Loughborough, LE11 3TU, UK.
E-mail addresses: A.Palmeri@Lboro.ac.uk, Dynamics.Structures@gmail.com (A. Palmeri).

https://doi.org/10.1016/j.probengmech.2022.103377
Received 1 March 2022; Received in revised form 24 October 2022; Accepted 28 October 2022
Available online 7 November 2022

accelerograms generated through stationary models tend to have a disproportionate number of cycles and, therefore, their energy content tends to be excessively high [6].

Moreover, recorded accelerograms could be better represented mathematically as samples of fully non-stationary stochastic processes, with variations in both time and frequency domains. In this context, temporal non-stationarity refers to the variation in the rate of change of the intensity of the ground motion over time; in contrast, spectral non-stationarity refers to the variation of the frequency content over time (e.g., [22–24]). Both variations are important and can dramatically affect the seismic response, especially when dealing with nonlinear structures. Several studies, including those reported in references [25–32], have addressed various theoretical and practical challenges associated with the joint time–frequency non-stationarity in recorded and stochastically generated accelerograms. These include the phenomenon of "moving resonance", the validity of pseudo-acceleration spectral ordinates as intensity measure of seismic ground motions compared to earthquake moment magnitude M_{w} and the distance R_{JB} from the seismic source to system site, the usefulness of fragilities based on ground accelerations scaled to have the same intensity measure, the sensitivities of seismic risk to different ground motion models. Furthermore, the availability of a detailed probabilistic model for the ground motion acceleration enables the application of random vibration methods to quantify the seismic response of amplitude- and frequency-dependent dynamic systems (e.g., [33–36]).

The simplest way to achieve temporal non-stationarity of spectrum-compatible accelerograms is by multiplying stationary samples by a conveniently selected modulating function. Less straightforward is the mathematical characterization of the artificial accelerograms as fully non-stationary random processes. Various methods have been proposed that modify recorded accelerograms so that the resulting response spectrum is somehow "compatible" with a target one. These methods are mainly based on the evaluation of a target evolutionary power spectral density (EPSD) function by means of recorded accelerograms (e.g., [37–40]) or by the decomposition of a recorded accelerogram into a number of wavelets (e.g., [41–43]).

A further class of stochastic approaches has been proposed by Spanos and associates (e.g., [44–46]), which does not require recorded accelerograms to define the temporal and spectral variation of the artificial accelerograms. Additionally, generalized harmonic wavelets have been utilized in an iterative procedure to improve the agreement of the mean response spectrum with the target one [47].

Many studies (e.g., [48–52]) have shown the importance of accurately modeling the non-stationary characteristics of ground motions to reliably assess the seismic response of nonlinear structures. In fact, an inaccurate estimate of the spectral contents may lead to severely underestimating or overestimating the expected level of dynamic response amplitudes. Comparatively, less attention has been paid to the effects that the generation of artificial accelerograms has on the variability of linear and nonlinear seismic responses. In fact, when artificial accelerograms are generated, two competing objectives should ideally be pursued: first, a target measure of the seismic action needs to be achieved "on average" (e.g., ±10% difference between the mean response spectrum and the target response spectrum); second, "just enough" sample-to-sample variability should be achieved, so that the generated suit of accelerograms covers the aleatory uncertainty of actual seismic events.

Motivated by the above considerations, this paper investigates the aleatory variability of linear and nonlinear seismic responses for two alternative strategies of stochastic simulation of artificial accelerograms. In both cases, a recorded accelerogram is assumed as a "parent signal", i.e., a random realization of a zero-mean Gaussian process, representative of the seismic action, from which a set of "child signals" can be generated.

In the first approach, the circular wavelet transform (CWT) is used to decompose the recorded accelerogram into the superposition of complex-valued harmonic wavelets with complex-valued combination coefficients, which are then randomized through a generalization of the well-known Shinozuka's formula [53–55]. In this case, different modeling choices operated in the frequency domain simultaneously affect the time-domain features of the generated accelerograms, and vice versa. Notwithstanding this, the wavelets' time- and frequency-localization capabilities can be used to efficiently manipulate a discrete signal. As an example, Cecini and Palmeri [56] [42,56] have used the CWT approach and the concept of the "time of maximum" (ToM) spectrum to devise a systematic procedure to match a target earthquake spectrum through iterative corrections that target specific frequency bands and time intervals.

In the second approach, the EPSD function is evaluated using the procedure recently proposed by Muscolino et al. [57], in which the time and frequency characteristics of the ground shaking model are calibrated separately. Furthermore, the present paper introduces a new, iterative stage to match the ordinates of a given earthquake spectrum.

Both methods treat parent and child signals as samples of a random process solely defined by the chosen parent signal; however, the two methods result in alternative definitions of the random process, and different choices in applying each technique tend to produce different results.

While the practical consequences of different modeling options are illustrated with a recorded accelerogram caused by a tectonic earthquake, the different methods of stochastic generations lend themselves to applications in other engineering fields where: (*i*) the relevant time series are affected by compounded time and frequency non-stationarities; and (*ii*) only a relatively small number of representative samples is available, e.g., non-synoptic winds gusts [58,59], fracking-induced earthquakes [60], turbulent liquid flows [61,62], heights of ocean waves [63], stress cycles in random fatigue processes [64,65], etcetera.

Elastic and constant-ductility inelastic response spectra are used to illustrate the variations and offer practical guidance to designers.

The key underpinning concepts and computational stages of the two stochastic generation methods are summarized in Sections 2 and 3, so to make the present paper self-contained. Furthermore, the practical applications of these methods is facilitated and improved by a new set of wavelet-based generation formulae (see Eqs. (4) to (6)), a more straightforward calibration of the slowly varying amplitude in the EPSD-based method (see Appendix B), and an additional spectrum-compatibilization procedure for the EPSD-based approach (see Section 3.2).

It is also worth emphasizing here that this paper's goal is not to compare the variability in terms of elastic and inelastic spectral ordinates coming from natural accelerograms with that achieved with artificial ones (e.g., [66]). Instead, the focus is on the inherent effects of two stochastic generation strategies that are somehow representative of two different and complementary approaches.

2. Wavelet-based generation of artificial accelerograms

The wavelet analysis consists of the mathematical representation of a given signal in terms of "wavelets", i.e., families of wave-like oscillating functions obtained by scaling and shifting a chosen function called "mother wavelet" (e.g., [67]). The "harmonic" and "musical" wavelets proposed by Newland [68–71] are particularly convenient for structural dynamics applications as their Fourier transform results in box-shaped functions. This property allows operating on a given frequency band of a signal without affecting other frequencies and makes wavelets particularly appealing in the seismic analysis of linear and nonlinear structures, e.g., in the case of base-isolated systems such as buildings, [72,73], rigid blocks, [73], water storage thanks [74], and nuclear reactor containment structures [75].

Let $f(t)$ be a non-periodic signal describing the ground acceleration over the finite time interval $[0, t_{\mathrm{d}}]$; and let $\Delta t = t_{\mathrm{d}}/(2N)$ be the sampling

time, such that the seismic signal is known at $2N+1$ discrete time instants $t_\ell = \ell\,\Delta t$, with $\ell = 1, 2, \ldots, 2N$; furthermore, $\omega_N = 2\pi\,N/t_\mathrm{d}$ is the Nyquist's frequency and $\Delta\omega = 2\pi/t_\mathrm{d}$ is the discretization step in the frequency domain.

A "circular" version of Newland's musical wavelets can be used [70] for the analysis of the parent signal $f(t)$. Circular wavelets are "wrapped" around the time interval of interest (without loss of generality, a unitary duration is assumed in Newland's original formulation). The seismic record $f(t_\ell)$ can then be expressed as the superposition of the complex-valued circular wavelets $\Psi_{j,k,\ell}$ and associated combination coefficients $\hat{a}_{j,k}$:

$$f(t_\ell) = 2\,\mathrm{Re}\left[\sum_{j=1}^{M}\sum_{k=0}^{b_j-1}\hat{a}_{j,k}\,\Psi_{j,k,\ell}\right], \tag{1}$$

in which the function $\mathrm{Re}[\cdot]$ returns the real value of the quantity within square brackets; M is the number of bands in which the frequency domain has been partitioned; b_j is the number of wavelets in the jth frequency band (corresponding to the number of discrete frequencies in the jth frequency band).

The generic wavelet appearing in the right-hand side of Eq. (1) can be expressed as:

$$\Psi_{j,k,\ell} = \frac{1}{b_j}\sum_{s=m_j}^{n_j-1}\exp\left[\imath\,\pi\,(2s+1)\left(\frac{\ell}{2N}-\frac{k}{b_j}\right)\right]. \tag{2}$$

It can be shown that $\Psi_{j,k,\ell}$ occupies the frequency band $\left[2\pi\,m_j/t_\mathrm{d},\,2\pi\,n_j/t_\mathrm{d}\right]$, with $0 \le m_j < n_j \le t_\mathrm{d}/(2\,\Delta t)$, and is centered at time $\tau_{j,k} = k\,t_\mathrm{d}/b_j$, with $b_j = n_j - m_j$. Furthermore, $\imath = \sqrt{-1}$ is the imaginary unit and $k = 0, \ldots, b_j - 1$ is a time index.

The combination coefficients $\hat{a}_{j,k}$ are calculated through a discrete convolution (e.g., [42]):

$$\hat{a}_{j,k} = \frac{b_j}{2N}\sum_{\ell=0}^{2N} f(t_\ell)\,\Psi^*_{j,k,\ell}, \tag{3}$$

where the superscripted asterisk means complex conjugate.

The randomization of the seismic signal $f(t_\ell)$ can be pursued through a generalization of the well-known Shinozuka's formula [54–56,76]. Accordingly, the rth child sample of the ground acceleration can be generated as:

$$\ddot{U}_\mathrm{g}^{(r)}(t_\ell) = 2\sum_{j=1}^{M}\frac{1}{b_j}\sum_{k=0}^{b_j-1}\left|\hat{a}_{j,k}\right|\times \sum_{s=m_j}^{n_j-1}\cos\left[\pi\,(2s+1)\left(\frac{\ell}{2N}-\frac{k}{b_j}\right)+\hat{\theta}_{j,k}+\phi_{j,k}^{(r)}\right], \tag{4}$$

where $\phi_{j,k}^{(r)}$ is the rth realization of a random variable uniformly distributed over the interval $[0, 2\pi[$ and $\hat{\theta}_{j,k} = \arg\left\{\hat{a}_{j,k}\right\}$ is the corresponding deterministic phase of the complex-valued coefficient of the parent signal.

Eq. (4) particularizes into the classical Shinozuka's formula for $M = N$, which implies $b_1 = b_2 = \cdots b_N = 1$ (i.e., each frequency band consists of a single discrete frequency), $m_j = j-1$, $n_j = j$ and $k = 0$ (i.e., there is no time localization, as there is only one wavelet in each frequency band). Accordingly, one obtains:

$$\begin{aligned}\ddot{U}_\mathrm{g}^{(r)}(t_\ell) &= \\ &= 2\sum_{j=1}^{N}\left|\hat{a}_{j,0}\right|\cos\left[\pi\,(2j-1)\left(\frac{\ell}{2N}\right)+\hat{\theta}_{j,0}+\phi_{j,0}^{(r)}\right] = \\ &= \sum_{j=1}^{N}A_j\cos\left(\omega_j^*\,t_\ell+\Phi_j^{(r)}\right),\end{aligned} \tag{5}$$

where $A_j = 2\left|\hat{a}_{j,0}\right|$, $\omega_j^* = (j-0.5)\,\Delta\omega$ and $\Phi_j^{(r)} = \hat{\theta}_{j,0}+\phi_{j,0}^{(r)}$ are the amplitude, circular frequency and random phase for the jth harmonic function, respectively.

The opposite choice in terms of possible trade-off between the fidelity of the non-stationary characteristics of the parent signal in the time and frequency domains would result in the use of a single frequency band. In this case, the particularization of Eq. (4) for $M = 1$ leads to:

$$\ddot{U}_\mathrm{g}^{(r)}(t_\ell) = \frac{2}{N}\sum_{k=0}^{N-1}\sum_{j=0}^{N-1}\left|\hat{a}_{1,k}\right| \times\cos\left[\pi\,(2j+1)\left(\frac{\ell}{2N}-\frac{k}{N}\right)+\hat{\theta}_{1,k}+\phi_{1,k}^{(r)}\right]. \tag{6}$$

It is worth emphasizing here that the Shinozuka's formula of Eq. (5) delivers samples of a stationary colored process, whose time-independent PSD function is entirely defined by the amplitude coefficients A_j; that is, the frequency content is fully preserved in the child samples but their amplitude is constant over time. On the contrary, it can be shown that the formula of Eq. (6) generates samples of an amplitude-modulated white noise, with cut-off frequency ω_N; that is, the time variation of the amplitude of the signal is preserved in the child signal, but no information is retained in the frequency domain (apart from the average intensity of the parent signal).

The generation formula of Eq. (4) is more general because it enables the user to retain partial information on the time and frequency domains. The implications of different partitioning of the frequency domain, i.e. different choices of the frequency bands b_j, with $j = 1, \ldots, M \le N$, will be explored in the numerical applications. It is important to note here that, because of the so-called Heisenberg's uncertainty principle (e.g., [67]), the more the time domain detail is enhanced in the wavelet representation of a discrete signal, the more the frequency one becomes poor, rising the need to find a compromise.

3. Generation via spectrum-compatible evolutionary PSD function

An alternative method for generating random samples of spectrum-compatible fully non-stationary zero-mean Gaussian processes has been recently proposed by Muscolino et al. [57] and is based on the use of a conveniently defined EPSD (evolutionary power spectral density) function. The main steps of this technique are summarized in the following subsections.

3.1. Evolutionary model of artificial accelerograms

Similar to the wavelet-based technique discussed in the previous section, Muscolino et al. [57] assume that a given recorded accelerogram is one of the infinite realizations of a fully non-stationary model of earthquake ground motion.

Mathematically, the latter is defined as the sum of zero-mean Gaussian uniformly modulated random processes. Each of these processes consists of the product of a non-negative deterministic modulating function, $A(t) \ge 0$, and a stationary zero-mean Gaussian filtered sub-process, $X_k(t)$. The function $A(t)$ has the units of an acceleration, e.g., $\left[\mathrm{m/s^2}\right]$ while the sub-process $X_k(t)$ is dimensionless.

The sought fully non-stationary stochastic process, $\ddot{U}_\mathrm{g}(t)$ is then obtained by dividing the time interval $\left[0, t_\mathrm{d}\right]$ into M contiguous sub-intervals of amplitude $\Delta T_k = s_k - s_{k-1}$, with $k = 1, 2, \ldots, M$, requiring that in each time interval the sub-process $X_k(t)$ possesses a uni-modal PSD function[1]; that is:

$$\ddot{U}_\mathrm{g}(t) = A(t)\sum_{k=1}^{M}X_k(t)\,W_k(t), \tag{7}$$

[1] The symbol M used in the wavelet-based generation (see Eqs. (1) and (4)) has a different meaning with respect to the one in the evolutionary PSD function (see Eq. (9)). In the first case, M is the number of frequency bands; in the second case, M is the number of uniformly modulated sub-processes.

where $W_k(t)$ is a deterministic window function, defined as:

$$W_k(t) = \begin{cases} 1\,, & \text{if } s_{k-1} \le t < s_k\,; \\ 0\,, & \text{otherwise}\,. \end{cases} \tag{8}$$

The resulting EPSD function of the piece-wise uniformly modulated random process is:

$$G_{\ddot{U}g}(\omega, t) = A^2(t) \sum_{k=1}^{M} W_k(t)\, G_k(\omega)\,, \tag{9}$$

where the kth sub-process $X_k(t)$ in the time interval $[s_{k-1}, s_k[$ is characterized by the following one-sided PSD function [57]:

$$G_k(\omega) = \beta_k \left(\frac{\omega^2}{\omega^2 + \omega_{\mathrm{H}k}^2} \right) \left(\frac{\omega_{\mathrm{L}k}^4}{\omega^4 + \omega_{\mathrm{L}k}^4} \right) G_k^{(\mathrm{CP})}(\omega)\,, \tag{10}$$

in which $\omega_{\mathrm{L}k}$ and $\omega_{\mathrm{H}k}$ are the kth frequency control of the second-order low-pass and first-order high-pass Butterworth filters, respectively.

Furthermore, $G_k^{(\mathrm{CP})}(\omega)$ is the uni-modal one-sided PSD function of the stationary random process introduced by Conte and Peng [77], which can be viewed as the linear combination of the displacement and velocity responses of a second-order SDoF (single degree of freedom) oscillator subjected to two statistically independent Gaussian white noise processes:

$$G_k^{(\mathrm{CP})}(\omega) = \frac{1}{\rho_k^2 + (\omega + \Omega_k)^2} + \frac{1}{\rho_k^2 + (\omega - \Omega_k)^2}\,, \tag{11}$$

where the parameters ρ_k and Ω_k are measures of the frequency bandwidth and "predominant" circular frequency of the kth stationary sub-process, respectively.

It can be shown that the peak of the PSD function $G_k^{(\mathrm{CP})}(\omega)$ occurs at:

$$\overline{\Omega}_k = \Omega_k \left[1 + \left(\frac{\rho_k}{\Omega_k} \right)^2 \right]^{1/4} \left[2 - \sqrt{1 + \left(\frac{\rho_k}{\Omega_k} \right)^2} \right]^{1/2}\,, \tag{12}$$

with $\overline{\Omega}_k > \Omega_k$.

Furthermore, the coefficient β_k introduced in Eq. (10) ensures that the stationary sub-process $X_k(t)$ possesses unit variance, i.e.:

$$\mathbb{E}\left\langle X_k^2(t) \right\rangle = \sigma_{Xk}^2 = \int_0^{+\infty} G_k(\omega)\, \mathrm{d}\omega = 1\,, \tag{13}$$

and can be calculated as:

$$\beta_k = \frac{2\,\rho_k}{\pi} \frac{\left(\omega_{\mathrm{H}k}^4 + \omega_{\mathrm{L}k}^4 \right) \bar{a}_k\, \bar{b}_k}{\omega_{\mathrm{L}k}^3 \left(\bar{c}_k + \bar{d}_k + \bar{e}_k \right)}\,, \tag{14}$$

in which:

$$\bar{a}_k = \left(\rho_k^2 + \Omega_k^2 \right)^4 + 2 \left(\rho_k^4 - 6\,\rho_k^2\,\Omega_k^2 + \Omega_k^4 \right) \omega_{\mathrm{L}k}^4 + \omega_{\mathrm{L}k}^8\,; \tag{15a}$$

$$\bar{b}_k = \rho_k^4 + 2\,\rho_k^2 \left(\Omega_k^2 - \omega_{\mathrm{H}k}^2 \right) + \left(\Omega_k^2 + \omega_{\mathrm{H}k}^2 \right)^2\,; \tag{15b}$$

$$\bar{c}_k = -2\,\bar{a}_k\,\rho_k\,\omega_{\mathrm{H}k}\,\omega_{\mathrm{L}k} \left(\rho_k^2 + \Omega_k^2 - \omega_{\mathrm{H}k}^2 \right)\,; \tag{15c}$$

$$\begin{aligned} \bar{d}_k = {} & \left\{ \left(\rho_k^2 + \Omega_k^2 \right)^2 \left(\rho_k^4 - 6\rho_k^2\Omega_k^2 + \Omega_k^4 + \omega_{\mathrm{L}k}^4 \right) \right. \\ & \left. - \omega_{\mathrm{H}k}^2 \left(\rho_k^2 - \Omega_k^2 \right) \left[\left(\rho_k^2 + \Omega_k^2 \right)^2 + \omega_{\mathrm{L}k}^4 \right] \right\} \\ & \times 2\,\omega_{\mathrm{L}k} \left(\omega_{\mathrm{H}k}^4 + \omega_{\mathrm{L}k}^4 \right)\,; \end{aligned} \tag{15d}$$

$$\begin{aligned} \bar{e}_k = {} & \sqrt{2}\,\bar{b}_k\,\rho_k \\ & \times \left\{ \omega_{\mathrm{L}k}^2 \left(\omega_{\mathrm{H}k}^2 - \omega_{\mathrm{L}k}^2 \right) \left(\omega_{\mathrm{L}k}^4 + \rho_k^4 - 2\,\rho_k^2\,\Omega_k^2 - 3\,\Omega_k^4 \right) \right. \\ & + \left(\omega_{\mathrm{H}k}^2 + \omega_{\mathrm{L}k}^2 \right) \left[\rho_k^6 + \Omega_k^6 + 3\,\Omega_k^2\,\rho_k^2 \left(\rho_k^2 + \Omega_k^2 \right) \right. \\ & \left. \left. + \omega_{\mathrm{L}k}^4 \left(\rho_k^2 - 3\,\Omega_k^2 \right) \right] \right\}\,. \end{aligned} \tag{15e}$$

It is worth mentioning here that in Eqs. (7) and (9), the deterministic function $A(t)$ is implicitly assumed to "slowly varying" compared with the stationary sub-processes $X_k(t)$ (see, e.g., [78]); that is, the Fourier transform of the amplitude $A(t)$ is expected to have energy content concentrated at frequencies that are much less than the predominant frequencies Ω_k of the sub-processes $X_k(t)$.

A satisfactory resemblance between the rth sample of the fully non-stationary stochastic process, $\ddot{U}_{\mathrm{g}}^{(r)}(t_\ell)$ and the recorded "parent signal", $f(t_\ell)$, can be achieved by separately fine-tuning the modulating function and the frequency content of the process $\ddot{U}_{\mathrm{g}}(t)$. This is a crucial difference with respect to the wavelet-based procedure summarized in the previous section, where an intervention in the time domain also affects the frequency domain, and vice versa. Appendices A and B detail the procedures that can be used to calibrate the parameters of the sub-processes $X_k(t)$ (Appendix A) and the modulating function $A(t)$ (Appendix B).

3.2. Generation of spectrum-compatible accelerograms

Once all the parameters characterizing the fully non-stationary zero-mean Gaussian process, $\ddot{U}_{\mathrm{g}}(t)$, defined in Eq. (7), are estimated (see Appendices A and B), the rth sample can be generated as:

$$\begin{aligned} \ddot{U}_{\mathrm{g}}^{(r)}(t) = {} & A(t) \sqrt{2\Delta\omega} \\ & \times \sum_{k=1}^{M} W_k(t) \sum_{j=1}^{N} \sqrt{G_k(j\,\Delta\omega)} \cos\left(j\,\Delta\omega\, t + \theta_j^{(r)} \right)\,, \end{aligned} \tag{16}$$

in which, similarly to the previous section, $\Delta\omega = 2\pi/t_{\mathrm{d}}$ is the discretization step in the frequency domain and $\omega_N = \pi/\Delta t$ is the upper cut-off circular frequency, equal to the Nyquist's frequency.[2] Furthermore, N is the number of the harmonic terms in the right-hand side of Eq. (16), given by $N = \omega_N/\Delta\omega = t_{\mathrm{d}}/(2\,\Delta t)$, and the random phase angles, $\theta_j^{(r)}$, are statistically independent and uniformly distributed over the interval $[0, 2\pi[$.

The procedure summarized in the previous subsections returns samples of a fully non-stationary random process, $\ddot{U}_{\mathrm{g}}^{(r)}(t)$, such that, in statistical sense, their cumulative intensity function $I_{\ddot{U}g}^{(r)}(t)$ (related to the evolutionary amplitude of the process) and zero-level up-crossing rate $\mathrm{d}Z_{\ddot{U}g}^{+(r)}(t)/\mathrm{d}t$ (related to the evolutionary frequency content of the process) closely match those of the parent signal, $f(t)$. In this respect, the parent signal can be viewed as a "credible" sample of the random process $\ddot{U}_{\mathrm{g}}(t)$.

However, the functions $I_{\ddot{U}g}(t)$ and $\mathrm{d}Z_{\ddot{U}g}^{+}(t)/\mathrm{d}t$ are not always sufficient to satisfactorily characterize the dynamic action for engineering applications. Instead, given the accelerogram $f(t)$, its elastic response spectrum in terms of displacements $S_{\mathrm{d}}^{(f)}(T_j, \zeta_0)$ (or, equivalently, in terms of pseudo-accelerations $S_{\mathrm{pa}}^{(f)}(T_j, \zeta_0) = \left(2\pi/T_j\right)^2 S_{\mathrm{d}}^{(f)}(T_j, \zeta_0)$) is commonly utilized to characterize the seismic input for analysis and design purposes.

Mathematically, the response spectrum is defined as the maximum absolute response of an SDoF quiescent oscillator with equivalent damping ratio ζ_0 (typically, $\zeta_0 = 0.05$) and undamped natural circular frequency ω_j (or undamped natural period $T_j = 2\pi/\omega_j$); that is:

$$S_{\mathrm{d}}^{(f)}(T_j, \zeta_0) = \max\left\{ \left| Q_j(t) \right|,\ 0 \le t \le t_{\mathrm{d}} \right\}\,, \tag{17a}$$

where $Q_j(t)$ is the solution of the following second-order differential equation:

$$\ddot{Q}_j(t) + 2\,\zeta_0\,\omega_j\,\dot{Q}_j(t) + \omega_j^2\,Q_j(t) = -f(t)\,. \tag{17b}$$

[2] As for the wavelet-based approach described in Section 2, the total number of discrete points in the time domain is $2N+1$, such that the signal's duration is $t_{\mathrm{d}} = 2N\,\Delta t$ and the Nyquist's frequency is $\omega_N = N\,\Delta\omega$.

In the case of the random process $\ddot{U}_g(t)$, if R samples are randomly simulated via Eq. (16), the mean generated spectrum can be defined as:

$$\overline{S}_d^{(R)}(T_j,\zeta_0) = \frac{1}{R}\sum_{r=1}^{R} S_d^{(r)}(T_j,\zeta_0)\,, \tag{18a}$$

where the superscript (R) reminds that the mean spectrum is calculated over R samples. The rth spectrum in the right-hand side of Eq. (18a) is given by:

$$S_d^{(r)}(T_j,\zeta_0) = \max\left\{\left|Q_j^{(r)}(t)\right|\,,\ \ 0\le t\le t_d\right\}\,, \tag{18b}$$

in which $Q_j^{(r)}(t)$ is the dynamic response to the rth sample of the random process $\ddot{U}_g(t)$:

$$\ddot{Q}_j^{(r)}(t) + 2\,\zeta_0\,\omega_j\,\dot{Q}_j^{(r)}(t) + \omega_j^2\,Q_j^{(r)}(t) = -\ddot{U}_g^{(r)}(t)\,. \tag{18c}$$

In general, a gap exists between the elastic response spectrum of the parent signal, $S_d^{(f)}(T_j,\zeta_0)$ (see Eq. (17a)), and the mean generated spectrum, $\overline{S}_d^{(R)}(T_j,\zeta_0)$ (see Eq. (18a)); that is:

$$\left|S_d^{(f)}(T_j,\zeta_0) - \overline{S}_d^{(R)}(T_j,\zeta_0)\right| = \varepsilon_j^{(R)}\,. \tag{19}$$

The discrepancy function appearing in the right-hand side of Eq. (19) can be reduced through an iterative procedure that modifies the frequency content of the stationary sub-processes $X_k(t)$ (e.g., [12]). Specifically, at the nth iteration, the kth PSD function becomes:

$$G_k^{(n)}\left(\omega_j\right) = g^{(n)}\left(\omega_j\right)\,G_k^{(n-1)}\left(\omega_j\right)\,, \tag{20a}$$

where the non-dimensional function $g^{(n)}\left(\omega_j\right)$ is a corrective term given by:

$$g^{(n)}\left(\omega_j\right) = g^{(n-1)}\left(\omega_j\right)\left[\frac{S_{pa}^{(f)}(T_j,\zeta_0)}{\overline{S}_{pa}^{(R,n-1)}(T_j,\zeta_0)}\right]^2\,, \tag{20b}$$

in which $\overline{S}_{pa}^{(R,n)}(T_j,\zeta_0)$ is the mean generated spectrum in terms of pseudo-accelerations as evaluated at the nth iteration. The iterative procedure begins with:

$$g^{(0)}\left(\omega_j\right) = 1\,, \tag{21a}$$

$$G_k^{(0)}\left(\omega_j\right) = G_k\left(\omega_j\right)\,, \tag{21b}$$

and

$$\overline{S}_{pa}^{(R,0)}(T_j,\zeta_0) = \omega_j^2\,\overline{S}_d^{(R)}(T_j,\zeta_0)\,. \tag{21c}$$

The method then proceeds with as many iterations as required to achieved the sought condition of spectrum compatibility. Very few iterations are usually needed to reduce the discrepancy function to an acceptable level for the frequencies (or periods) of interests, i.e.:

$$\begin{aligned}\varepsilon_j^{(R,n)} &= \left|S_d^{(f)}(T_j,\zeta_0) - \overline{S}_d^{(R,n)}(T_j,\zeta_0)\right| \\ &\le \text{tolerance}\,;\end{aligned} \tag{22}$$

usually, no more than four iterations are required.

At the nth iteration, the samples of the non-stationary process are evaluated as:

$$\begin{aligned}\ddot{U}_g^{(r,n)}(t) = {} & A(t)\sqrt{2\Delta\omega}\sum_{k=1}^{M} W_k(t) \\ & \times \sum_{j=1}^{N}\sqrt{G_k^{(n)}\left(j\,\Delta\omega\right)}\cos\left(j\,\Delta\omega\,t + \theta_j^{(r)}\right)\,.\end{aligned} \tag{23}$$

Once the iterative procedure is terminated, the samples $\ddot{U}_g^{(r,n)}(t)$ are baseline corrected (e.g., [79–82]). Specifically, a best-fit polynomial curve of order ≥ 2 is determined for each child sample through a least-squares regression analysis and is then subtracted from the acceleration time history, so that: (i) the end ground velocity is zero, i.e., $\dot{U}_g^{(r,n)}(t_d) = 0$; and (ii) any physically inconsistent "trends" in the slowly varying moving-average of the ground displacement time history is removed.

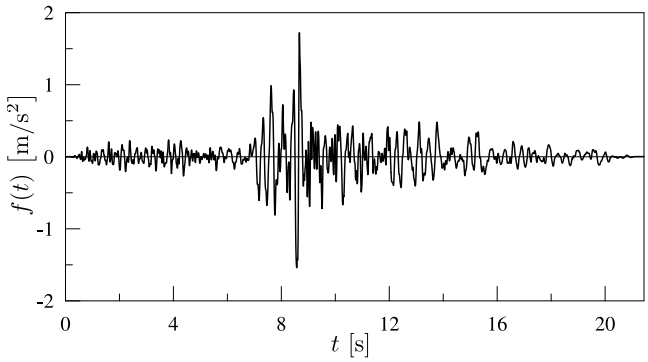

Fig. 1. Case-study accelerogram (i.e., the "parent signal"): 1983 Trinidad offshore earthquake.

In general, the fully non-stationary process so obtained after n iterations does not simultaneously satisfy the compatibility in terms of cumulative intensity function $I_f(t)$, zero-level up-crossing rate $\mathrm{d}Z_f^+(t)/\mathrm{d}t$ and elastic response spectrum $S_d^{(f)}(T_j,\zeta_0)$; however, it delivers a satisfactory compromise for engineering applications.

In fact, the spectrum-compatibilization procedure has been summarized in this subsection to demonstrate the potential of the EPSD-based method to generate child samples that match a target spectrum while simultaneously preserving some of the joint time–frequency characteristics of a recorded accelerogram. As the present study focuses on comparing two different stochastic generation techniques, entering the details of which spectra should the child signals be compatibilized to is behind the scope of the paper. However, potential applications include cases of forensic earthquake engineering [83,84], the seismic performance assessment of structures under a maximum credible event [85], the generation of artificial accelerograms compatible with conditional earthquake spectra [86–92], etcetera.

4. Results and discussion

This section compares the performance of the two generation methods presented in the previous two sections.

Results are presented and discussed first for the EPSD-based stochastic generation method (Section 3), as this approach has two main parameters that independently control the smoothness of the amplitude function of the ground acceleration, $A(t)$ (via the moving-average window width $\widehat{\Delta t}$), and the number M of uniformly modulated sub-processes $X_k(t)$. Thus, a great degree of versatility is evidenced.

By contrast, the results of the wavelet-based method depend on a single choice, i.e., the subdivision of the frequency domain in a number M of frequency bands. For the sake of simplicity, the formulation presented in Section 2 entails frequency bands with an equal number of discrete frequencies b_j.

In addition to the cumulative intensity, zero-level up-crossing rate and elastic response spectra, the last part of this section compares the generated samples in terms of inelastic response spectra, so to quantify the effects of different methods and different generation parameters on the nonlinear seismic response of structures.

4.1. Case-study accelerogram

For both generation methods, the "parent signal" has been chosen as the first horizontal component (azimuth angle= 0°) of the ground acceleration recorded at the "Rio Dell Overpass, E Ground" station during the 1983 Trinidad offshore earthquake. The selected signal, depicted in Fig. 1, has been downloaded from the PEER database [93]

Table 1
Main time and frequency properties of the case-study accelerogram.

t_d [s]	Δt [s]	N	ω_N [rad/s]	$\Delta\omega$ [rad/s]
21.44	0.005	2144	628.32	0.29

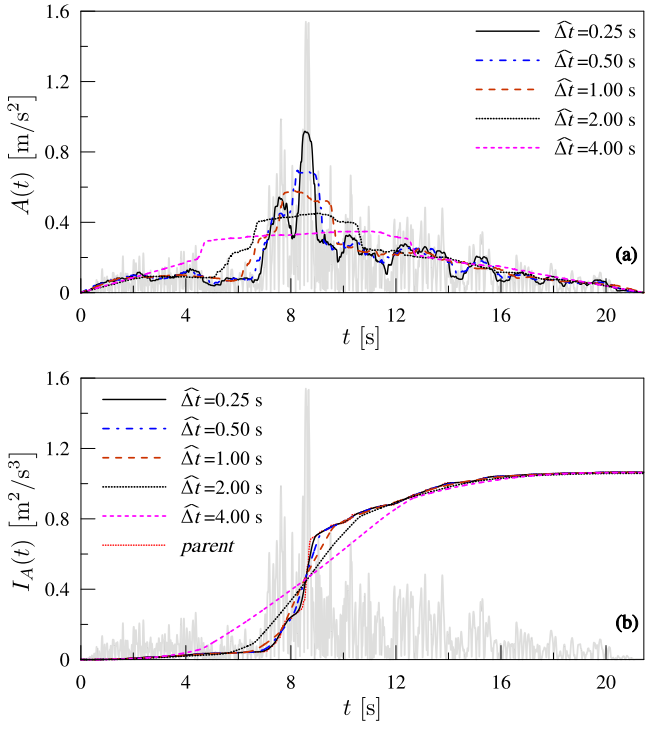

Fig. 2. Absolute value of the parent accelerogram (gray line) compared with: (a) modulating functions $A(t)$ obtained for five different time windows $\widehat{\Delta t}$; (b) cumulative intensity $I_f(t)$ of the recorded accelerogram (i.e., the "parent", red dotted line) and cumulative intensities for the five time windows $I_A(t)$. (For interpretation of the references to color in this figure legend, the reader is referred to the web version of this article.)

and is characterized by moment magnitude $M_w = 5.7$ and a Joyner–Boore site-to-source distance $R_{JB} = 68.02$ km. The main time and frequency properties of the signal are shown in Table 1.

4.2. Evolutionary PSD method

As described in Section 3, this method of stochastic generation defines the fully non-stationary process $\ddot{U}_g(t)$ as the sum of M time-windowed uniformly modulated Gaussian processes, each one given by a deterministic modulating function, $A(t)$, multiplied by a stationary zero-mean sub-process, $X_k(t)$.

4.2.1. Modulating function $A(t)$

The time variation of the amplitude of the generated samples is obtained through an appropriate estimation of the modulating function $A(t)$, which in turn depends on the cumulative intensity $I_f(t)$ of the parent signal (see Eqs. (B.3) to (B.5)).

Different modulating functions can be obtained by varying the moving time window $\widehat{\Delta t} = 2\,p\,\Delta t$ in Eq. (B.5). In the chosen case-study application, five different values of $\widehat{\Delta t}$ have been assumed, varying between 0.25 and 4.00 s and corresponding to a number of $2\,p$ time intervals between 50 and 800. The resulting modulating functions are shown in Fig. 2(a) together with the absolute value of the parent signal (gray line).

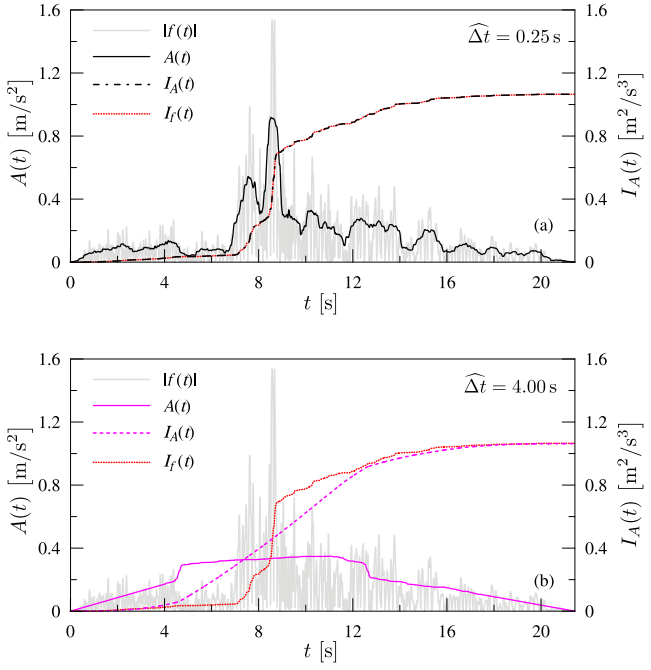

Fig. 3. Modulating function $A(t)$, cumulative intensity of the parent signal $I_f(t)$ and cumulative intensity of the modulating function $I_A(t)$ for the time windows (a) $\widehat{\Delta t} = 0.25$ s and (b) $\widehat{\Delta t} = 4.00$ s – The absolute value of the parent signal, $|f(t)|$, is plotted with a light-gray solid line. (For interpretation of the references to color in this figure legend, the reader is referred to the web version of this article.)

In Fig. 2(b), the cumulative intensity of the parent signal, $I_f(t)$ (see Eq. (B.1)), is compared against the cumulative intensity of the modulating function, i.e., the integral of the squared modulating function, $I_A(t)$, so defined:

$$I_A(t) = \int_0^t A^2(\tau)\,\mathrm{d}\tau\,, \tag{24}$$

The smaller the value of the moving time window $\widehat{\Delta t}$, the closer the match between $I_f(t)$ and $I_A(t)$, as the two curves tend to coincide for $\widehat{\Delta t} \to 0$. Noticeably, while differences between $I_f(t)$ and $I_A(t)$ are clearly discernible for $\widehat{\Delta t} \geq 2.00$ s, the final values always coincide, i.e., $I_f(t_d) = I_A(t_d)$ irrespectively of the value of $\widehat{\Delta t}$, meaning that the total energy of the parent signal is preserved regardless of the smoothing applied to its intensity function.

For the sake of clarity, Fig. 3 further illustrates the effects of choosing a relatively small moving time window (i.e., $\widehat{\Delta t} = 0.25$ s) and a relatively large one (i.e., $\widehat{\Delta t} = 4.00$ s) by plotting against each other (*i*) the absolute values of the parent accelerogram $|f(t)|$ (light gray solid lines), (*ii*) its cumulative intensity, $I_f(t)$ (red lines), (*iii*) the modulating functions $A(t)$ (solid lines, black for $\widehat{\Delta t} = 0.25$ s and pink for $\widehat{\Delta t} = 4.00$ s), and (*iv*) the corresponding cumulative intensities, $I_A(t)$ (dashed lines, again black and pink depending on the value of the moving time window $\widehat{\Delta t}$). It can be observed that:

- For $\widehat{\Delta t} = 0.25$ s, i.e. $p = 25$ (Fig. 3(a)), $I_A(t)$ closely matches $I_f(t)$ as the two lines are almost indistinguishable; the downside is that the associated modulating function $A(t)$ of the random process $\ddot{U}_g(t)$ is not smooth, showing several "high-frequency" fluctuations. This is undesirable, as a clear separation should occur between the frequency contents of the random process $\ddot{U}_g(t)$ and its "slowly varying" modulating function $A(t)$, as this is the assumption underpinning the definition of the piecewise uniformly modulated random process $\ddot{U}_g(t)$ via Eqs. (7) and (9).
- On the contrary, for $\widehat{\Delta t} = 4.00$ s, i.e., $p = 400$ (Fig. 3(b)), the modulating function $A(t)$ appears smooth and does not show any

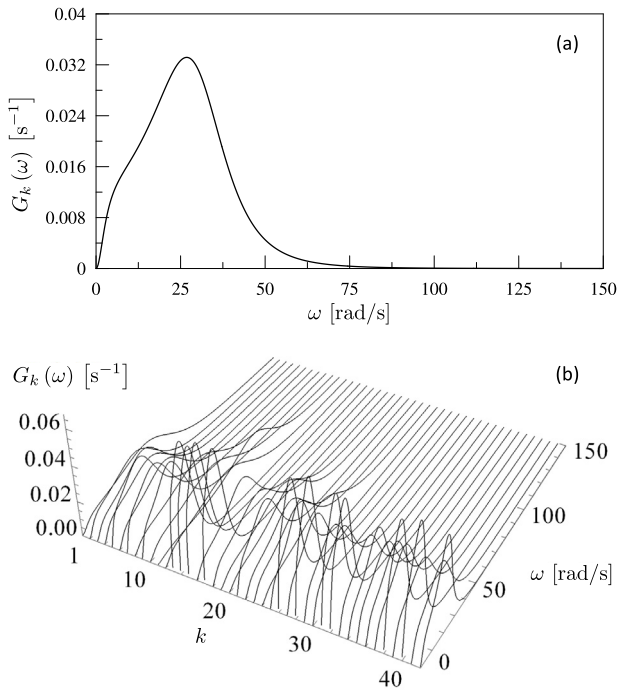

Fig. 4. One-sided PSD functions of the case-study accelerograms for (a) only one time interval and (b) $M = 42$ time intervals.

apparent high-frequency fluctuations; on the adverse side, however, the sharp peak at about $t = 8.50$ s has disappeared from the modulating function, meaning that no significant concentration of energy occurs around that time instant; rather, the energy is spread almost uniformly between 4.50 and 12.50 s, meaning that highly nonlinear structures, e.g. rocking or sliding systems, might experience completely different dynamic responses when exposed to the parent signal $f(t)$ or any of the child signals $\ddot{U}_g^{(r)}(t)$.

4.2.2. Spectral parameters of the sub-processes $X_k(t)$

According to Muscolino et al. [57], the evolutionary frequency content of the model detailed in Section 3 (see Eqs. (10) and (11)) can be calibrated by using readily available data such as the number of peaks, P_{fk}, and zero-level up-crossings, Z_{fk}^+, in the kth time interval ΔT_k (see Eqs. (A.1) and (A.2)).

The larger the number M of the time intervals ΔT_k, the closer the resulting random process $\ddot{U}_g(t)$ will closely match, on average, the salient frequency characteristics of the parent signal $f(t)$.

To illustrate this point and, more generally, to investigate the effects of subdividing the duration of the parent accelerogram into different numbers of time intervals, two extreme conditions have been considered for the case-study accelerogram, namely:

- $M = 1$, i.e., a single sub-process $X_1(t)$ is used for the whole duration of the signal ($\Delta T_1 = t_d$), meaning that the whole random process $\ddot{U}_g(t)$ is uniformly modulated; and
- $M = 42$, corresponding to time intervals with equal duration $\Delta T_k = 0.5$ s for $k \leq M - 1$ and $\Delta T_M = t_d - (M-1)\Delta T_1 = 0.94$ s, which allow tracking very closely the evolutionary energy content of the parent signal.

The parameters required for the characterization of the one-sided PSD functions $G_k(\omega)$ are reported in Tables 2 and 3 for $M = 1$ and $M = 42$, respectively. The resulting plots are shown in Figs. 4(a) and (b), respectively.

Table 2
Model parameters of the one-sided PSD function $G_1(\omega)$ for $M = 1$ and $\Delta T_1 = t_d = 21.44$ s.

k	Z_{fk}^+	P_{fk}	ΔT_k [s]	Ω_k [rad/s]	ρ_k [rad/s]	ω_{Hk} [rad/s]	ω_{Lk} [rad/s]	β_k
1	101	173	21.44	29.6	14.6	2.9	41.3	8.2

Table 3
Model parameters of the one-sided PSD function $G_k(\omega)$ for $M = 42$.

k	Z_{fk}^+	P_{fk}	ΔT_k [s]	Ω_k [rad/s]	ρ_k [rad/s]	ω_{Hk} [rad/s]	ω_{Lk} [rad/s]	β_k
1	4	8	0.50	50.3	26.9	5.0	71.8	15.2
2	3	7	0.50	37.7	21.5	3.8	54.9	12.2
3	3	5	0.50	37.7	18.3	3.8	52.3	10.3
4	3	7	0.50	37.7	21.5	3.8	54.9	12.2
5	2	6	0.50	25.1	15.6	2.5	37.6	8.8
6	3	6	0.50	37.7	20.2	3.8	53.8	11.4
7	2	7	0.50	25.1	16.1	2.5	38.1	9.2
8	4	7	0.50	50.3	25.1	5.0	70.4	14.1
9	2	4	0.50	25.1	13.5	2.5	35.9	7.6
10	4	8	0.50	50.3	26.9	5.0	71.8	15.2
11	6	6	0.50	75.4	21.5	7.5	92.6	12.0
12	4	8	0.50	50.3	26.9	5.0	71.8	15.2
13	1	6	0.50	12.6	8.8	1.3	19.6	5.1
14	1	8	0.50	12.6	9.1	1.3	19.8	5.2
15	1	4	0.50	12.6	8.3	1.3	19.2	4.7
16	3	4	0.50	37.7	15.5	3.8	50.1	8.6
17	1	4	0.50	12.6	8.3	1.3	19.2	4.7
18	3	6	0.50	37.7	20.2	3.8	53.8	11.4
19	4	6	0.50	50.3	22.7	5.0	68.4	12.7
20	4	5	0.50	50.3	19.4	5.0	65.8	10.8
21	2	5	0.50	25.1	14.7	2.5	36.9	8.3
22	3	5	0.50	37.7	18.3	3.8	52.3	10.3
23	3	5	0.50	37.7	18.3	3.8	52.3	10.3
24	4	7	0.50	50.3	25.1	5.0	70.4	14.1
25	2	3	0.50	25.1	11.4	2.5	34.2	6.4
26	1	5	0.50	12.6	8.6	1.3	19.5	4.9
27	2	4	0.50	25.1	13.5	2.5	35.9	7.6
28	1	3	0.50	12.6	7.8	1.3	18.8	4.4
29	2	6	0.50	25.1	15.6	2.5	37.6	8.8
30	2	5	0.50	25.1	14.7	2.5	36.9	8.3
31	1	5	0.50	12.6	8.6	1.3	19.5	4.9
32	1	6	0.50	12.6	8.8	1.3	19.6	5.1
33	2	5	0.50	25.1	14.7	2.5	36.9	8.3
34	2	3	0.50	25.1	11.4	2.5	34.2	6.4
35	2	5	0.50	25.1	14.7	2.5	36.9	8.3
36	2	4	0.50	25.1	13.5	2.5	35.9	7.6
37	2	4	0.50	25.1	13.5	2.5	35.9	7.6
38	1	7	0.50	12.6	9.0	1.3	19.7	5.1
39	2	7	0.50	25.1	16.1	2.5	38.1	9.2
40	1	4	0.50	12.6	8.3	1.3	19.2	4.7
41	2	5	0.50	25.1	14.7	2.5	36.9	8.3
42	3	4	0.94	20.1	8.2	2.0	26.6	4.6

4.2.3. Fully non-stationary samples

In the previous subsections, the role played by moving time window $\hat{\Delta t}$ and number of time subdivision intervals M in the mathematical definition of the EPSD function for the case-study accelerogram has been discussed. In the following, the compound effects arising from a combination of different choices for these two modeling parameters are investigated. Specifically, four cases have been analyzed, corresponding to the combination of extreme cases, as detailed below:

(a) Modulating function $A(t)$ with moving time window $\hat{\Delta t} = 4.00$ s and only one sub-process $X_1(t)$, i.e., $M = 1$ and $\Delta T_1 = 21.44$ s;
(b) same modulating function as in the previous case, i.e., $\hat{\Delta t} = 4.00$ s, and forty-two sub-process $X_k(t)$, i.e., $M = 42$, $\Delta T_1 = \Delta T_2 = \cdots \Delta T_{41} = 0.50$ s and $\Delta T_{42} = 0.94$ s (see Table 3);
(c) modulating function with $\hat{\Delta t} = 0.25$ s and $M = 1$;
(d) modulating function with $\hat{\Delta t} = 0.25$ s and $M = 42$.

Fig. 5 allows a visual comparison of the EPSD functions returned by the application of Eq. (9) for the four cases listed above. In particular,

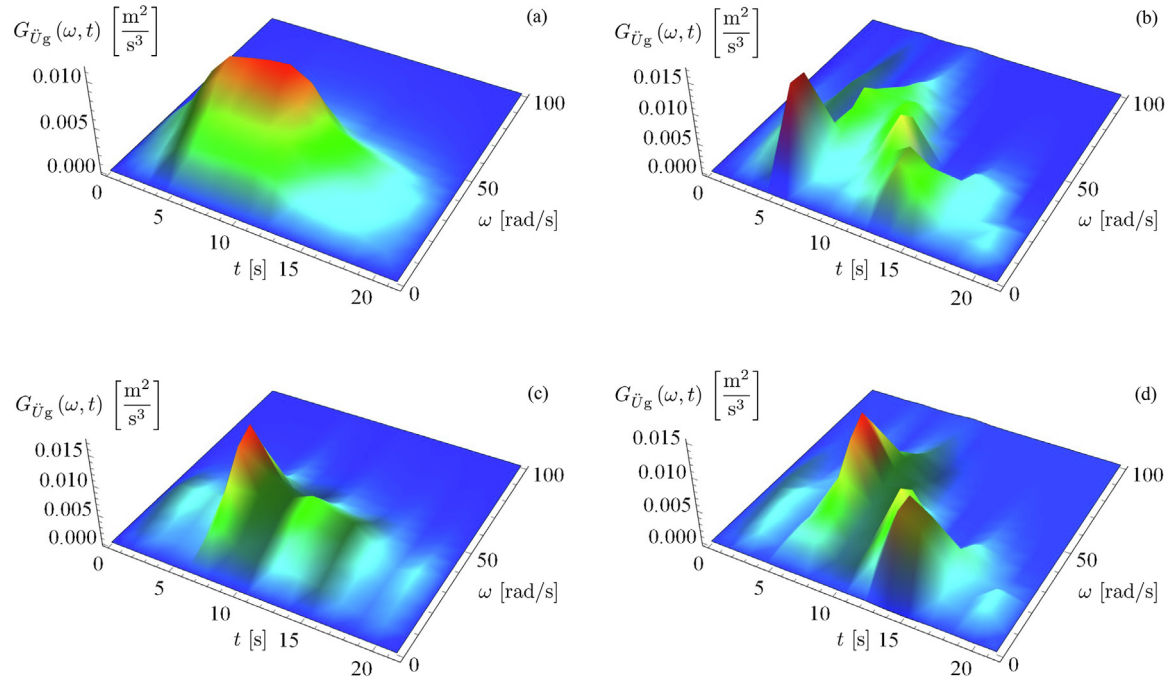

Fig. 5. Joint time–frequency representation of the evolutionary PSD functions obtained varying the time window $\hat{\Delta t}$ for the modulating function $A(t)$ and the subdivision of the parent signal in M time intervals: (a) $\hat{\Delta t} = 4.00\,\text{s}$ and $M = 1$; (b) $\hat{\Delta t} = 4.00\,\text{s}$ and $M = 42$; (c) $\hat{\Delta t} = 0.25\,\text{s}$ and $M = 1$; (d) $\hat{\Delta t} = 0.25\,\text{s}$ and $M = 42$.

Figs. 5(a) and (c) show that, for $M = 1$, each cross-section of the EPSD function $G_{\ddot{U}_g}(\omega,t)$ taken orthogonality to the time axis t is "self similar" to the PSD function depicted in Fig. 4(a), with all the ordinates proportionally scaled by the deterministic function $A(t)$, which in turn depends on the width of the time smoothing window $\hat{\Delta t}$. Accordingly, at any time instant $t \in [0, t_d]$, the energy content is maximum around the same frequency $\overline{\Omega}_1 = 29.4\,\text{rad/s}$. Conversely, the EPSD functions in Figs. 5(b) and (d), obtained for $M = 42$, show that the frequency $\overline{\Omega}_k$ changes significantly over time.

Once all the parameters characterizing the fully non-stationary Gaussian process $\ddot{U}_g(t)$ are estimated, Eq. (16) can be used to generate the required samples. Importantly, that the rth realization of the jth random phase angle $\theta_j^{(r)}$ appearing in Eq. (16) is the same for all time intervals ΔT_k; that is, there are no sudden jumps in the phase of the harmonic contributions to the generic sample $\ddot{U}_g^{(r)}(t)$ at the interface between two consecutive time intervals ΔT_k and ΔT_{k+1}.

Using this approach, a set of $R = 100$ samples has been generated for each of the four modeling cases. Fig. 6 compares the cumulative intensity function $I_f(t)$ of the parent signal (red line) against those of the child signals. Specifically, the black dashed lines are the mean value of the functions $I_{\ddot{U}_g}^{(r)}(t)$ obtained for the R generated samples; that is:

$$\overline{I_{\ddot{U}_g}}(t) = \frac{1}{R}\sum_{r=1}^{R} I_{\ddot{U}_g}^{(r)}(t) = \frac{1}{R}\sum_{r=1}^{R}\int_0^t \left[\ddot{U}_g^{(r)}(\tau)\right]^2 \mathrm{d}\tau\,. \tag{25}$$

Furthermore, the black solid lines define the empirical confidence intervals for mean plus/minus one standard deviation; finally, the gray shadowed areas define the envelope of the R random realizations.

In Figs. 6(a) and (b), the trend of the mean cumulative intensity functions, $\overline{I_{\ddot{U}_g}}(t)$, evaluated with a moving window $\hat{\Delta t} = 4.00\,\text{s}$, shows significant differences with respect to the deterministic one for the parent signal, $I_f(t)$. However, the final values at $t = t_d$ are very close to each other. Furthermore, Figs. 6(c) and (d) show that reducing the moving time window to $\hat{\Delta t} = 0.25\,\text{s}$ has the effect to close the gap between the functions $\overline{I_{\ddot{U}_g}}(t)$ and $I_f(t)$.

For the same four modeling choices, a similar set of comparisons as in Fig. 6 is offered in Fig. 7, this time in terms of the zero-level up-crossings. In Figs. 7(a) and (c), a linear trend can be observed for the mean function $\overline{Z_{\ddot{U}_g}^+}(t)$, defined as the mean value of the realizations of the cumulative up-crossing functions for the generated child signals; that is:

$$\overline{Z_{\ddot{U}_g}^+}(t) = \frac{1}{R}\sum_{r=1}^{R} Z_{\ddot{U}_g}^{+(r)}(t)\,. \tag{26}$$

The observed linear trend is consistent with the adoption of a single time subdivision, i.e., $M = 1$, in Eq. (16), meaning that the same expected zero-level up-crossing rate is assumed for the whole duration of the signal. This linear trend is significantly different with respect to deterministic function evaluated for the parent signal (red lines). The plots of the functions $\overline{Z_{\ddot{U}_g}^+}(t)$ (mean for the child signals) and $Z_f^+(t)$ (parent signal) appear closer in Figs. 7(b) and 7(d), where the results are presented for the subdivision of the time duration t_d in $M = 42$ intervals.

4.2.4. Spectrum-compatible fully non-stationary samples

To satisfy the spectrum compatibility between the mean elastic response spectrum for the artificially generated accelerograms, $\overline{S}_{pa}^{(R)}(T_j, \zeta_0)$, and the elastic response spectrum of the parent accelerogram, $S_{pa}^{(f)}(T_j, \zeta_0)$, the compatibilization procedure summarized in Section 3.2 has been applied with $n = 3$ iterations. Four different sets of spectrum-adjusted accelerograms have been generated through Eq. (23), i.e., one for each of the four combinations of moving time window $\hat{\Delta t}$ and number of time subdivisions M analyzed above. In all cases, the viscous damping ratio $\zeta_0 = 0.05$ has been assumed.

Fig. 8 compares the parent signal (red line) with generic child samples for each of the four combinations of the governing parameters $\left\{\hat{\Delta t}, M\right\}$. The comparison is shown for both: (*i*) the samples $\ddot{U}_g^{(r)}(t)$, generated via Eq. (16) and plotted with gray lines; and (*ii*) the spectrum-compatibilized samples $\ddot{U}_g^{(r,n)}(t)$, generated for $n = 3$ via Eq. (23) and plotted with black lines. As expected, the child samples for $\left\{\hat{\Delta t} = 0.25\,\text{s}, M = 42\right\}$ (Fig. 8(d)) are remarkably similar to the parent signal (more than all the other cases). Furthermore, the amplitudes of the spectrum-adjusted samples (black lines) tend to be higher than those generated at the 0th iteration (gray lines). This happens because,

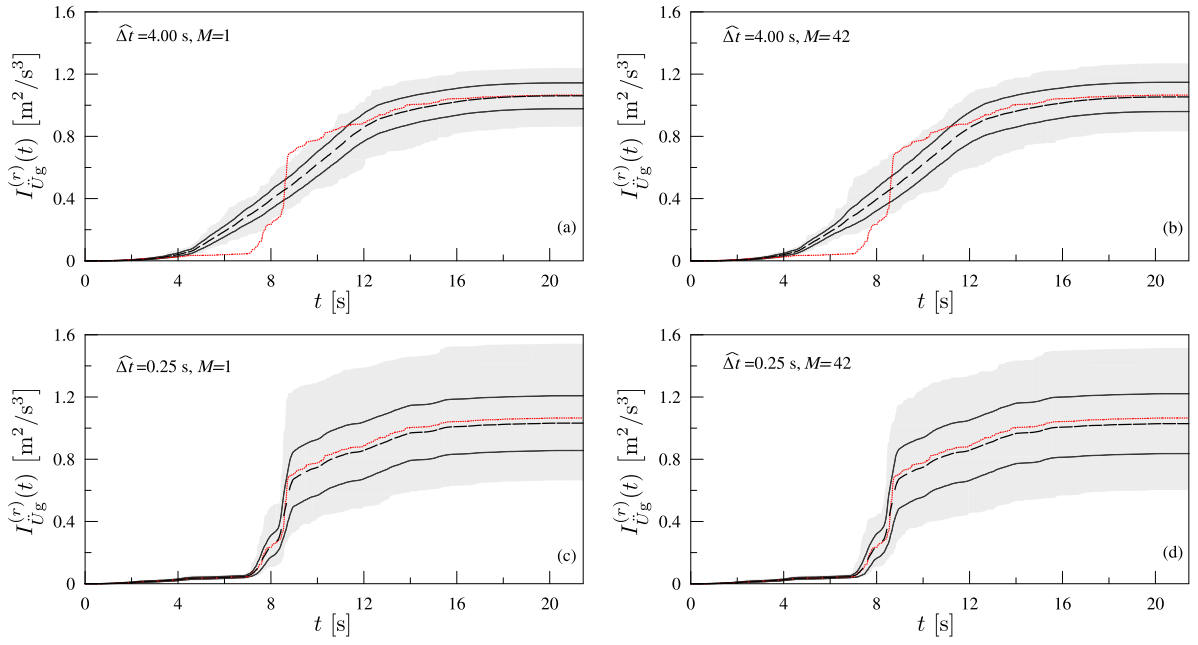

Fig. 6. Cumulative intensity functions $I_f(t)$ of the parent signal (red line) and child signals for different combinations of moving time window $\widehat{\Delta t}$ and number M of time subdivisions (mean value, black dashed line; mean ± one standard deviation, black solid lines; envelope of maximum and minimum values for whole set of generated signals, gray shaded area). (For interpretation of the references to color in this figure legend, the reader is referred to the web version of this article.)

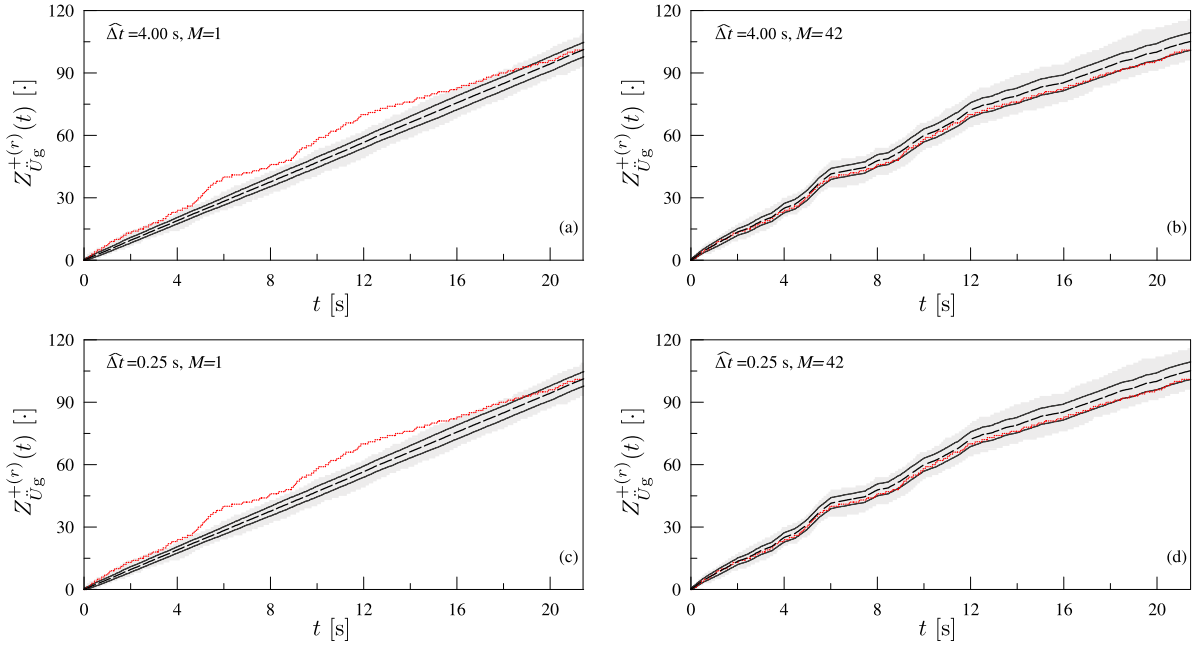

Fig. 7. Cumulative zero level up-crossings $Z^+_f(t)$ of the parent signal (red line) and child signals for different combinations of moving time window $\widehat{\Delta t}$ and number M of time subdivisions (mean value, black dashed line; mean ± one standard deviation, black solid lines; envelope of maximum and minimum values for whole set of generated signals, gray shaded area). (For interpretation of the references to color in this figure legend, the reader is referred to the web version of this article.)

typically, energy is added to the child signals through the iterations required to achieve the compatibility with the target spectrum.

The mean values of the cumulative intensity functions, $\overline{I_{\ddot{U}g}}(t)$, and cumulative zero-level up-crossing functions, $\overline{Z^+_{\ddot{U}g}}(t)$, of the spectrum-adjusted samples are depicted in Figs. 9(a) and 9(b), respectively, and compared against their deterministic counterparts for the parent signal (red lines).

Interestingly (see Fig. 9(a)), the spectrum-compatibilization procedure increases the cumulative intensity of the child signals, as more energy is required to match the response spectrum of the parent signal. Furthermore, the adoption of a large moving time window $\widehat{\Delta t}$ results in a disproportionate increase in the cumulative intensity of the child signals; that is, for $\widehat{\Delta t} = 4.00$ s the final value of the cumulative intensity is such that $\overline{I_{\ddot{U}g}}(t_d) > 2\, I_f(t_d)$. The overshooting of $I_f(t_d)$ is much less for $\widehat{\Delta t} = 0.25$ s.

In Fig. 10, the average spectra of the initial sets of artificial accelerograms are plotted (0th iteration, black dashed lines; 3rd iteration, black solid lines) and compared against the deterministic spectrum of the parent accelerogram (red lines). It can be observed that for all the four combinations of $\widehat{\Delta t}$ and number of time subdivisions M, the elastic

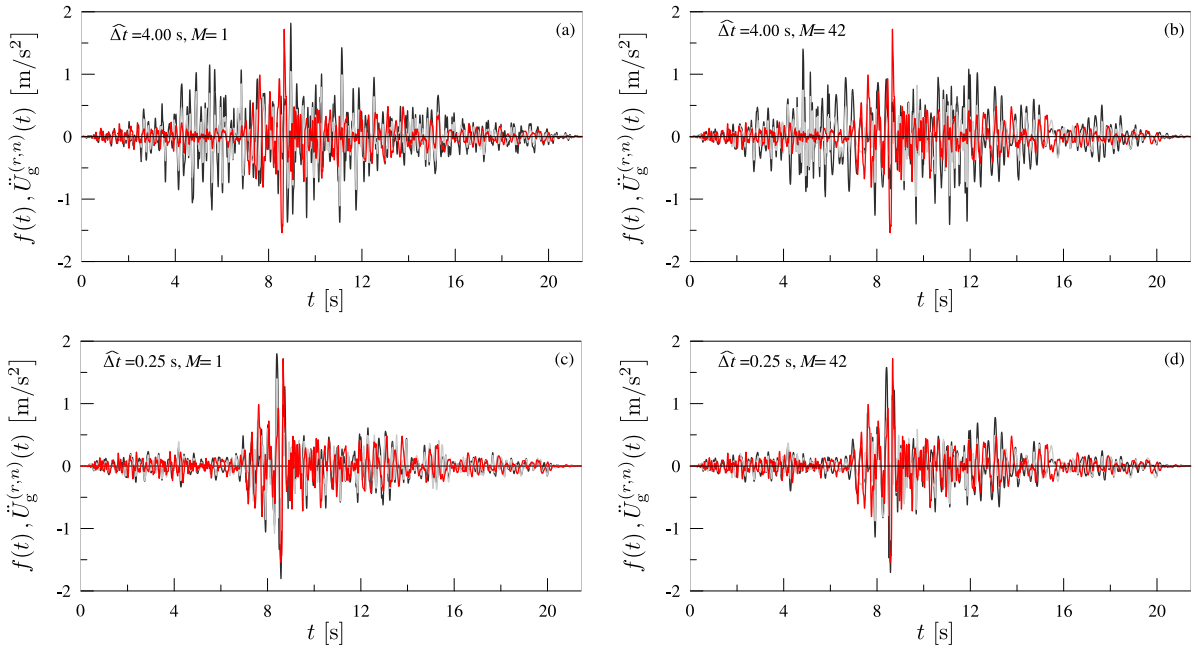

Fig. 8. Comparison among the parent accelerogram (red line) and the rth generated sample by the proposed EPSD-based method, considering different combinations of moving time window $\widehat{\Delta t}$ and number M of time subdivisions – 0th iteration (gray line), and 3rd spectrum-compatibilization iteration (black line). (For interpretation of the references to color in this figure legend, the reader is referred to the web version of this article.)

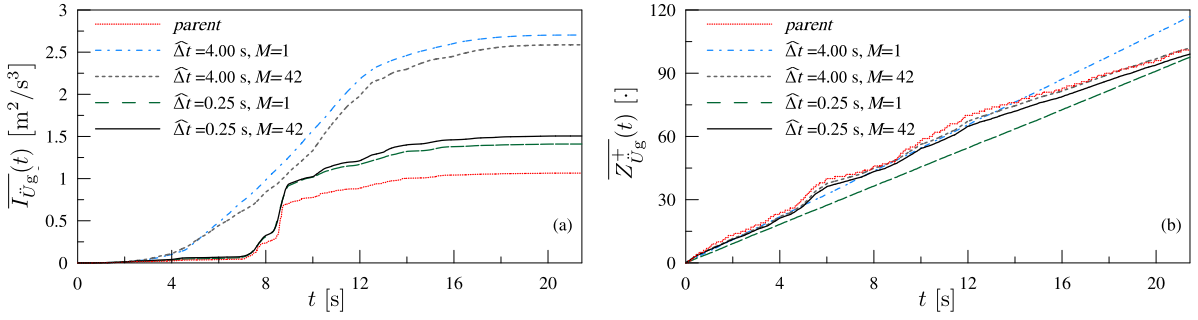

Fig. 9. Cumulative functions representing the intensity, $I_f(t)$ (a), and the zero-level up-crossing, $Z_f^+(t)$ (b), of the parent signal (red line) compared to the corresponding mean values obtained for four sets of $R = 100$ child samples after $n = 3$ iterations of spectrum-compatibilization; each set is obtained for a different combination of moving time window $\widehat{\Delta t}$ and number M of time subdivisions. (For interpretation of the references to color in this figure legend, the reader is referred to the web version of this article.)

response spectrum at the third compatibilization iteration is in very good agreement with the parent one.

4.3. Wavelet-based generation

By using the wavelet-based method described in Section 2, three different randomization schemes have been investigated to highlight how the trade-off between localizations in time and frequency domains plays a fundamental role for the purpose of generating meaningful time histories of ground accelerations. The three selected schemes correspond to $M = 1$, 42, and 2144 frequency bands of equal bandwidth.

Fig. 11 compares three generic child signals obtained through Eq. (4) (black lines) with the parent signal (red lines). As the number M of frequency bands increases, the fidelity in mimicking the frequency content of the parent signal improves but at the same time, due to Heisenberg's uncertainty principle, the accuracy in preserving the evolutionary amplitude of the parent signal deteriorates.

It can be shown that for the limiting case $M = 1$ (Fig. 11(a)) corresponds to a white noise uniformly modulated by the amplitude of the parent signal (i.e., no information preserved in the frequency domain), while the opposite limiting case $M = 2144$ (Fig. 11(c)) corresponds to a stationary colored noise with the same PSD function as the parent signal (i.e., no information preserved in the time domain).

In Figs. 12 to 14, a comparison is presented in terms of cumulative intensity functions $I_{\ddot{U}\mathrm{g}}(t)$, cumulative zero-level up-crossing functions $Z^+_{\ddot{U}\mathrm{g}}(t)$ and elastic response spectra in terms of acceleration, $S_{\mathrm{a}}(T_j, \zeta_0)$; the latter quantity is defined as the maximum absolute value of the absolute acceleration of a linear SDoF oscillator with period of vibration T_j and viscous damping ratio $\zeta_0 = 0.05$; that is:

$$S_{\mathrm{a}}^{(f)}(T_j,\zeta_0) = \max\left\{\left|Q_j(t)+f(t)\right|,\ 0\le t\le t_{\mathrm{d}}\right\} \approx S_{\mathrm{pa}}^{(f)}(T_j,\zeta_0)\,, \tag{27}$$

where reference is made to the notation adopted in Sub Section 3.2.

In detail, Figs. 12(a), 13(a) and 14(a) compares the parent and mean generated functions for the three subdivisions of the frequency domain, i.e., $M = 1$, 42 and 2144. For each subdivisions, $R = 100$ child signals have been generated. The intermediate number of frequency bands, $M = 42$, has been chosen because the corresponding bandwidth of the resulting frequency bands is $\omega_N/M = 628.3/42 \approx 15$ rad/s, which provides enough granularity in the frequency domain. The other Sub-figures (b), (c) and (d) deepen the comparison by plotting each

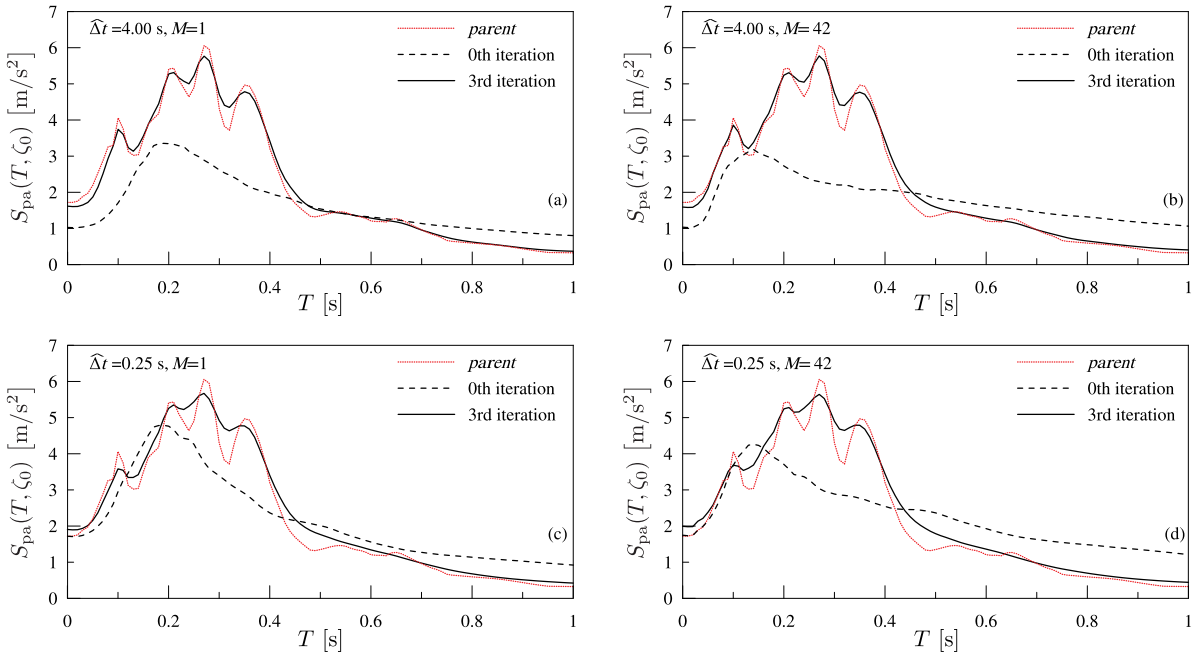

Fig. 10. Effects of the spectrum-compatibilization on the child signals obtained for different combinations of $\widehat{\Delta t}$ and M. The mean values of the pseudo-acceleration response spectra at the 0th (dashed black line) and 3rd iteration (solid black line) have been calculated with $R = 100$ child samples. (For interpretation of the references to color in this figure legend, the reader is referred to the web version of this article.)

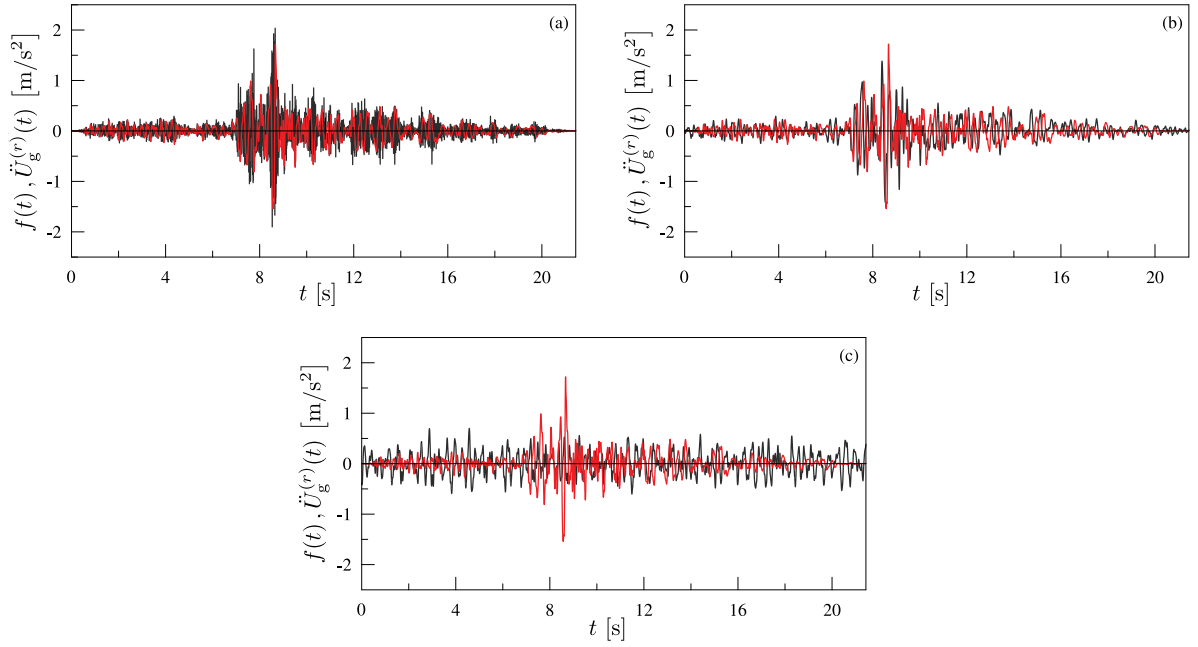

Fig. 11. Comparison among the parent accelerogram (red line) and the rth generated sample by the proposed wavelets-based method, considering a subdivision of the frequency domain into (a) $M = 1$, (b) $M = 42$, and (c) $M = 2144$ frequencies bands. (For interpretation of the references to color in this figure legend, the reader is referred to the web version of this article.)

deterministic function $I_{\ddot{U}\mathrm{g}}(t)$, $Z^{+}_{\ddot{U}\mathrm{g}}(t)$ and $S_{\mathrm{a}}(T_j,\zeta_0)$ against the corresponding statistics, namely: (i) mean value (dashed lines); (ii) bounds of the confidence interval corresponding to mean plus/minus one standard deviation (solid lines); (iii) maximum–minimum envelope of the generated signals (shadowed areas).

For the first limiting case, i.e., $M = 1$, the cumulative intensity function (black line in Fig. 12(a)) is in very good agreement with the parent one (red line) while the zero-level up-crossing function (black line in Fig. 13(a)) heavily overestimate the parent one (red line). In fact, with a single frequency band, the child signals are uniformly modulated samples of a white noise, with a far larger number of high-frequency fluctuations.

The opposite situation occurs in the second limiting case, i.e., $M = 2144$ (gray dotted lines in Figs. 12(a) and 13(a)). In fact, with a single

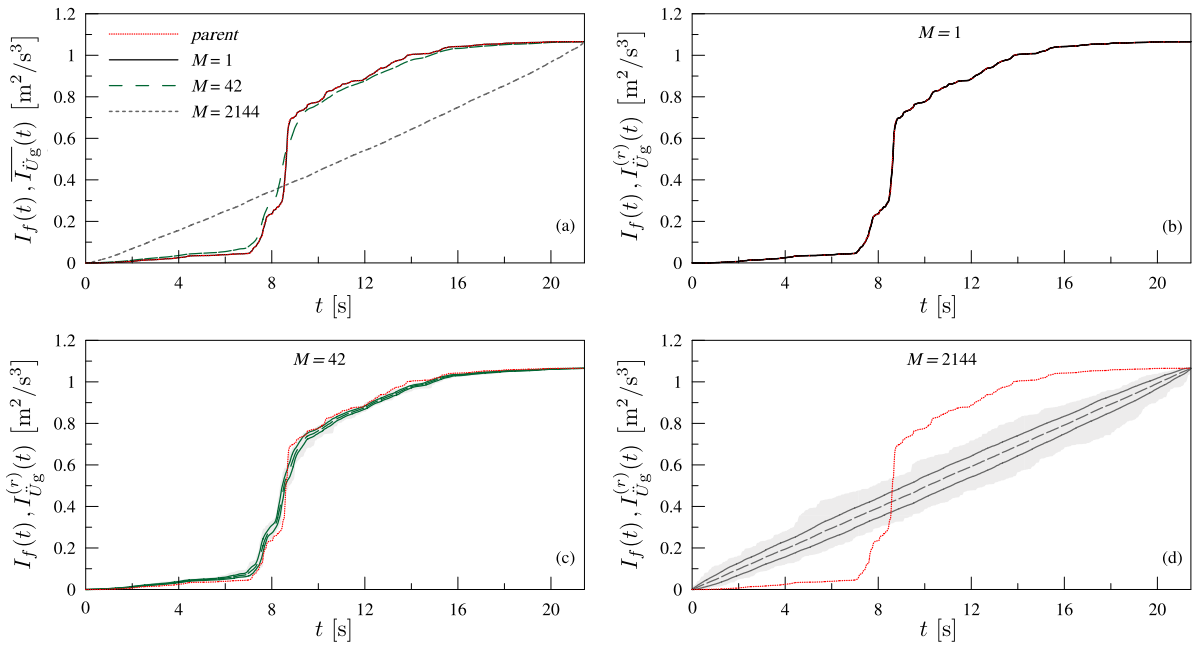

Fig. 12. Wavelet-based generation — Parent cumulative intensity function, $I_f(t)$ (red line), compared against mean functions for an increasing number M of frequency bands (a) and against further statistics (b, c, d); mean value, dashed line; mean value ± one standard deviation, solid lines; minimum–maximum envelope, shaded areas. (For interpretation of the references to color in this figure legend, the reader is referred to the web version of this article.)

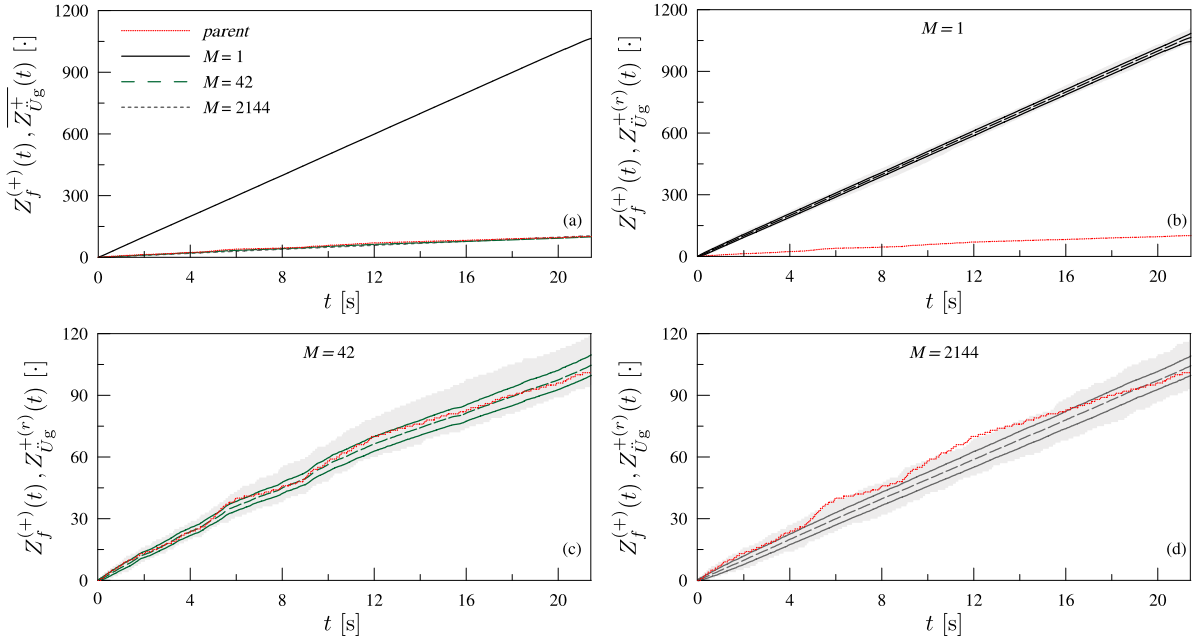

Fig. 13. Wavelet-based generation — Parent cumulative zero-level up-crossing function $Z_f^{(+)}(t)$ (red line), compared against mean functions for an increasing number M of frequency bands (a) and against further statistics (b, c, d); mean value, dashed line; mean value ± one standard deviation, solid lines; minimum–maximum envelope, shaded areas. (For interpretation of the references to color in this figure legend, the reader is referred to the web version of this article.)

discrete frequency in each frequency band, no time localizations are possible, meaning that the child signals are samples of a stationary random process with an expected linear trend in the cumulative intensity function.

If follows that an intermediate case, e.g., $M = 42$, should be used to generate child signals whose characteristics are sufficiently close to those of the parent signal in both the time domain and the frequency domain.

This consideration is confirmed by the elastic response spectra plotted in Fig. 14. Among the three schemes considered in this numerical application, only the case $M = 42$ delivers a set of response spectra that are in a good agreement with that of the parent accelerogram (see Fig. 14(c)). Incidentally, it is worth mentioning here that while in the wavelet-based method there is only one parameter controlling the characteristics of the generated samples, i.e. the number of frequency bands M, with direct implications on both the time and the frequency domain, the EPSD-based method has two independent parameters that can be used to fine-tune the generation, i.e., the moving time window $\widehat{\Delta t}$ (mainly affecting the time domain) and the number of time subdivisions M (mainly affecting the frequency domain).

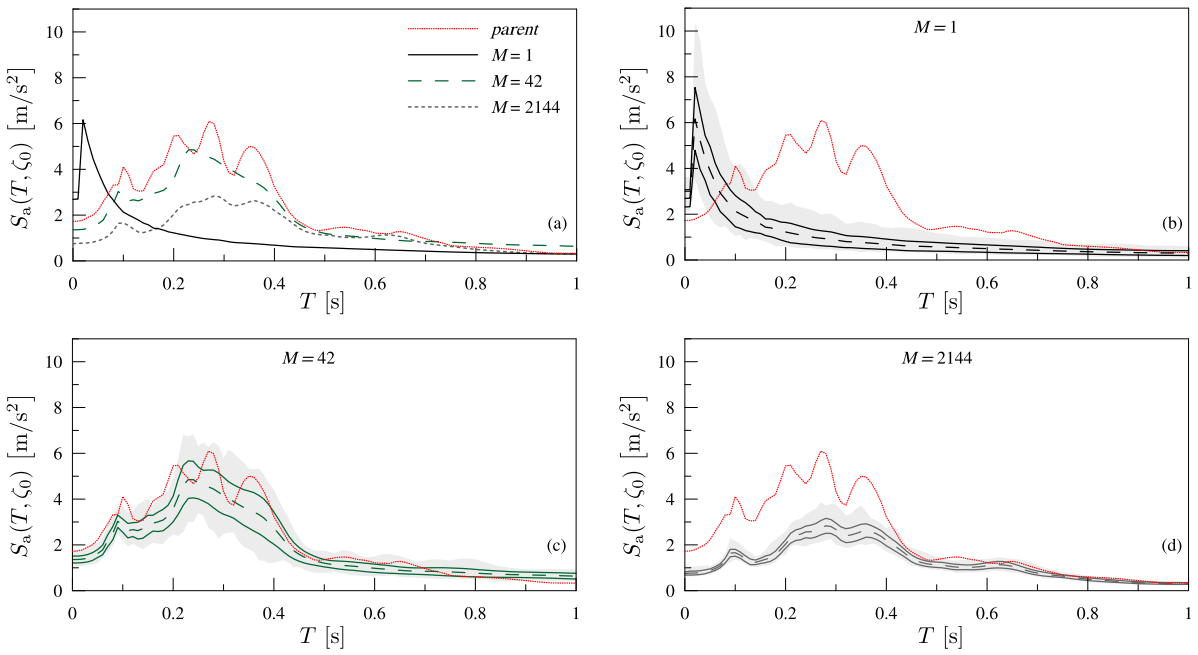

Fig. 14. Wavelet-based generation — Parent elastic response spectrum (viscous damping ratio: $\zeta_0 = 0.05$) in terms of absolute accelerations, $S_a^{(f)}(T)$ (red line), compared against mean spectra for an increasing number M of frequency bands (a) and against further statistics (b, c, d); mean value, dashed line; mean value ± one standard deviation, solid lines; minimum–maximum envelope, shaded areas. (For interpretation of the references to color in this figure legend, the reader is referred to the web version of this article.)

4.4. Nonlinear dynamic analyses

In this subsection, inelastic response spectra have been computed to investigate the effects of the two generation methods (wavelet- and EPSD-based) on the seismic response on nonlinear structural systems. Specifically, the case of elastic-perfectly plastic SDoF oscillators has been considered. All the nonlinear spectra have been computed using the commercial software SeismoSpect 2022, assuming viscous damping ratio $\zeta_0 = 0.05$ and ductility factor demand $\mu = 5$.

In Figs. 15 and 16, the inelastic acceleration spectrum of the parent signal (red lines) is plotted against the spectra obtained with seven sets of $R = 100$ child signals each (four sets for the EPSD-based method, corresponding to different combinations of moving time window $\widehat{\Delta t}$ and number M of time subdivisions; three sets for the wavelet-based method, corresponding to $M = 1$, 42 and 2144). These figures show that generation method and choice of the governing parameters can have profound effects on the nonlinear seismic responses to the generated child signals. Furthermore, the magnitude of these effects can be higher than in the case of linear seismic response.

For the EPSD-based method, the choice of governing parameters appears to be particularly important for the inelastic response spectra of fairly "rigid" structures (i.e., with period of vibration T less than 0.40 s, see Fig. 15). Furthermore, at least for the selected case-study earthquake record, the results are more influenced by the moving time window $\widehat{\Delta t}$ than by the number M of sub-processes. This is also because the procedure of spectrum compatibilization tends to apply similar modifications to the frequency content of the child signals independently of the number M of subdivisions (see Eqs. (20) to (23)).

For the wavelet-based method, it appears that only an intermediate value of the number of frequency bands, e.g., $M = 42$, can deliver credible statistics in terms of nonlinear seismic responses. In fact, the two limiting cases $M = 1$ and $M = 2144$ produce inelastic spectra that are very far from the parent one.

5. Conclusions

The definition of the seismic action plays a fundamental role in the analysis of earthquake-resistant structures, especially if they are designed to exceed the linear-elastic range under severe ground motions. It follows that any computational model of seismic excitation adopted in practice should be as realistic as possible, therefore including the effects of time-varying intensity and frequency content of the ground shaking. In practice, it is necessary to implement stochastic excitation models that explicitly account for the full non-stationary characteristics observed in recorded accelerograms.

In this paper, the effects of time-varying intensity and frequency content on the elastic and inelastic spectra of artificially generated earthquake ground motions are investigated. Two alternative stochastic methods are used to generate sets of artificial accelerograms with temporal and spectral non-stationarity similar to those of a recorded signal, i.e., a "parent signal", deemed to be representative of the seismic hazard.

The wavelet-based method, presented in Section 2, exploits the wavelet transform and consists of random phase angle rotations of the circular wavelets used to represent the parent signal. This approach enables the generation of fully non-stationary "child" samples without the need to define the evolutionary power spectral density (EPSD) function of the ground acceleration. The other method, on the contrary, requires the EPSD evaluation of the parent signal by means the procedure recently proposed by Muscolino et al. [57], appropriately modified in this paper.

The numerical results have evidenced that the most crucial step in the wavelet-based method is a suitable choice of the bands to divide the frequency domain. It has been shown that using too few or too many frequency bands leads to child signals totally different from the parent one. This is due to the loss of fidelity in either the time or frequency domain, thus confirming the importance of accurately representing the seismic input in both domains. For the chosen case-study signal, a division of the frequency domain into $M = 42$ bands provides an acceptable accuracy in both domains. Importantly, improving the accuracy in the frequency domain by using a larger number of frequency bands for the circular wavelets results in a simultaneous loss of accuracy in the time domain. The opposite happens when the number of the frequency bands reduces. In the present paper, the frequency domain has been uniformly partitioned into intervals of equal bandwidth. Current investigations are looking at the increased efficiency that can be achieved when frequency intervals of different bandwidths are used, e.g., partitioning the frequency domain into interval possessing the same energy.

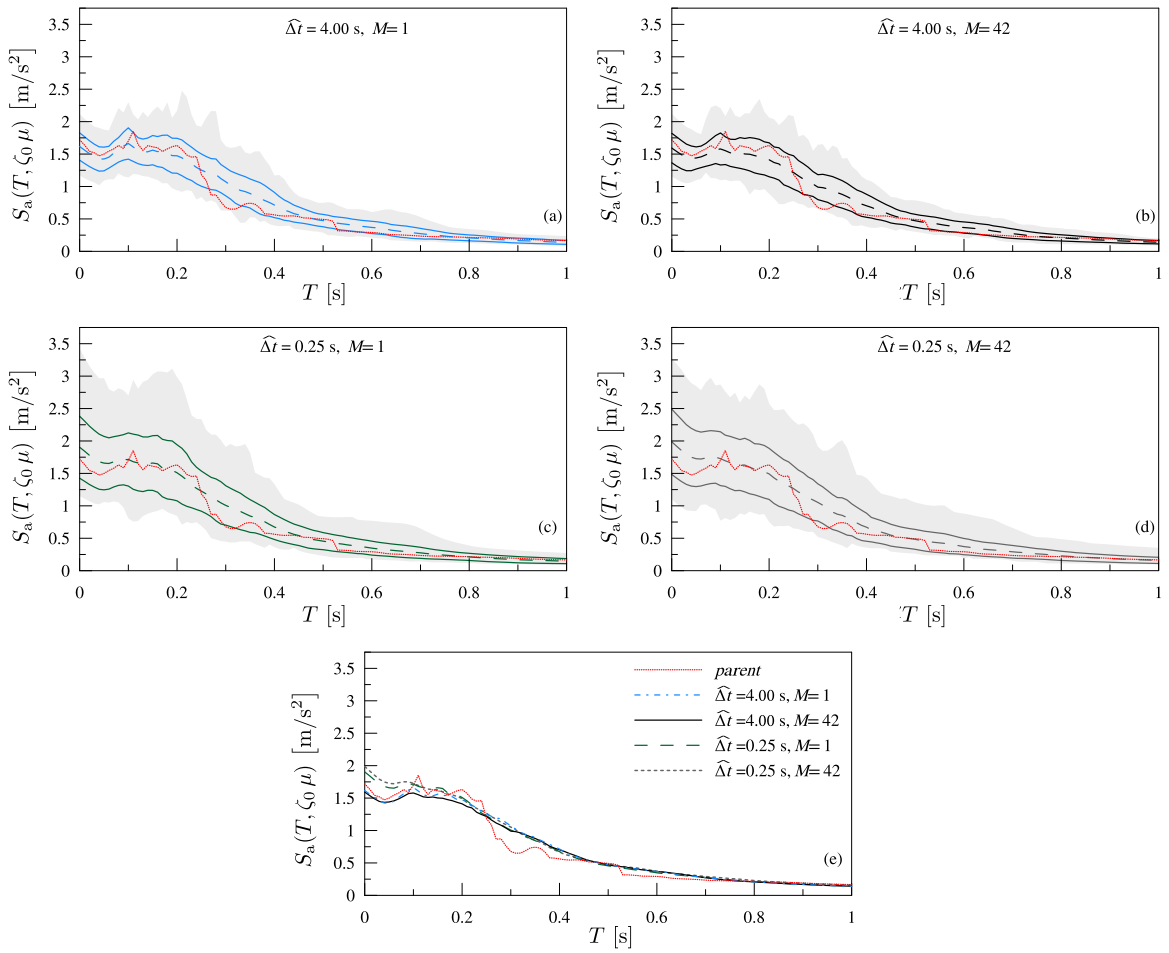

Fig. 15. EPSD-based method — Parent inelastic response spectrum (viscous damping ratio: $\zeta_0 = 0.05$; ductility demand: $\mu = 5$) in terms of absolute accelerations, $S_a^{(f)}(T, \zeta_0 = 0.05; \mu = 5)$ (red line), compared against mean spectra for different combinations of the governing parameters $\widehat{\Delta t}$ and M (e) and against statistics for each combination (a, b, c, d); mean value, dashed line; mean value ± one standard deviation, solid lines; minimum–maximum envelope, shaded areas. (For interpretation of the references to color in this figure legend, the reader is referred to the web version of this article.)

By contrast, the application of iterative corrections in the so-called EPSD-based method allows the recorded acceleration spectrum to fall into the confidence interval evaluated as the mean value plus/minus one standard deviation of the generated samples. It has also been shown that the choice of the modulating function, strictly related to the variation in time of the intensity of the case-study accelerogram, is particularly significative for both the elastic and elastoplastic response spectra.

Further research is needed to ascertain the effects of other governing parameters on the generation of child samples, e.g., the adoption of a correlation structure for the random phases utilized in the wavelet-based method (in the present study, all the random phases are assumed to be statistically independent). Additional types of nonlinearities should also be considered, including the cases of rocking and sliding systems. Finally, the generation methods should be tested for a range of recorded accelerograms with different characteristics, e.g., in terms of magnitude of the seismic event, distance to the source and soil type, so to quantify the expected sample-to-sample variability in the child signals generated in various circumstances.

Declaration of competing interest

The authors declare that they have no known competing financial interests or personal relationships that could have appeared to influence the work reported in this paper.

Data availability

Data will be made available on request.

Appendix A. Calibration of the spectral parameters of the sub-processes $X_k(t)$

Once the time interval duration of the recorded accelerogram, $[0, t_d]$, is divided in n contiguous time intervals (not necessarily of the same duration $\Delta T_k = t_d/n$), the one-sided PSD function $G_k(\omega)$ of the stationary sub-process $X_k(t)$ can be characterized by defining its predominant circular frequency and circular frequency bandwidth as:

$$\Omega_k = \frac{2\pi Z_{fk}^+}{\Delta T_k}; \tag{A.1a}$$

$$\rho_k = \frac{\pi Z_{fk}^+}{2\Delta T_k}\left[\pi - 2\frac{Z_{fk}^+}{P_{fk}}\right], \tag{A.1b}$$

where Z_{fk}^+ and P_{fk} are the number of zero-level up-crossings and the number of peaks of the parent signal $f(t)$ in the time intervals, $[s_{k-1}, s_k[$, with $s_0 = 0$, $s_n = t_d$ and $s_k = s_{k-1} + \Delta T_k$. Furthermore, the control frequencies of the kth pair of Butterworth filters in the time interval $[s_{k-1}, s_k[$ are given by:

$$\omega_{Hk} = 0.1\,\Omega_k; \tag{A.2a}$$

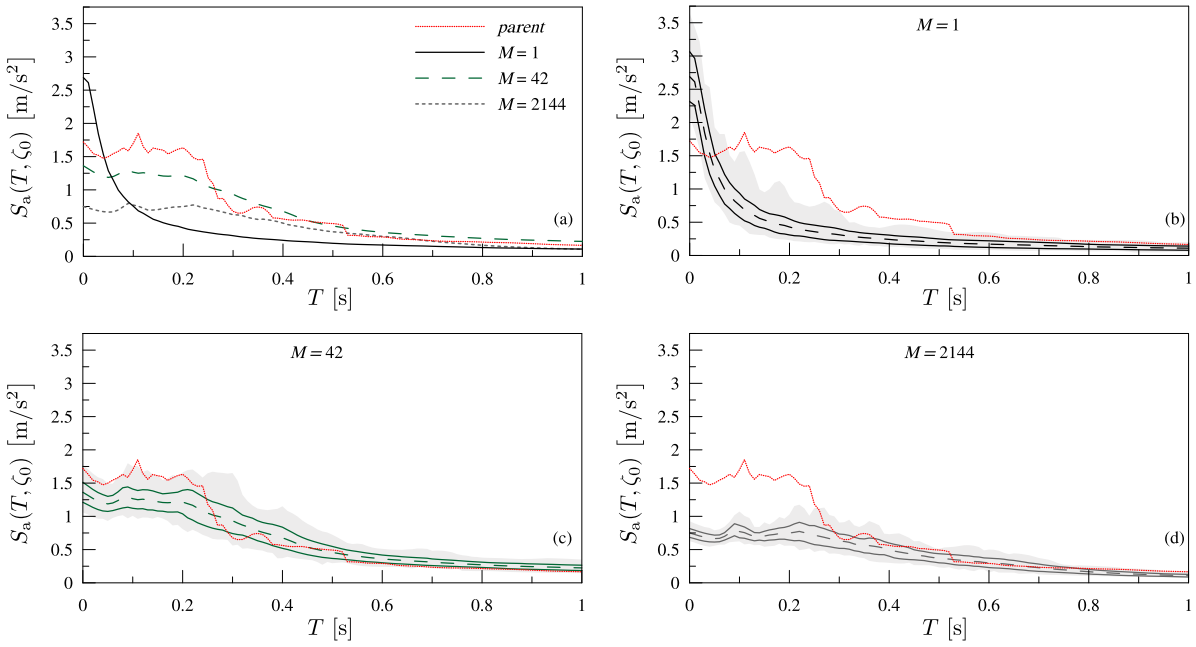

Fig. 16. Wavelet-based generation – Parent inelastic response spectrum (viscous damping ratio: $\zeta_0 = 0.05$; ductility demand: $\mu = 5$) in terms of absolute accelerations, $S_a^{(f)}(T,\zeta_0 = 0.05;\mu = 5)$ (red line), compared against mean spectra for an increasing number M of frequency bands (a) and against further statistics (b, c, d); mean value, dashed line; mean value ± one standard deviation, solid lines; minimum–maximum envelope, shaded areas. (For interpretation of the references to color in this figure legend, the reader is referred to the web version of this article.)

$$\omega_{Lk} = \Omega_k + 0.8\,\rho_k\,. \tag{A.2b}$$

Appendix B. Calibration of the modulating function $A(t)$

First, the deterministic cumulative intensity function of the parent accelerogram, $f(t)$, is evaluated as:

$$I_f(t) = \int_0^t f^2(\tau)\,\mathrm{d}\tau\,, \tag{B.1}$$

with $0 \le t \le t_d$.

Owing to the unit variance of the stationary sub-process $X_k(t)$, the expected cumulative intensity of the fully non-stationary stochastic process $\ddot{U}_g(t)$ can be evaluated as:

$$\begin{aligned}\mathbb{E}\left\langle I_{\ddot{U}g}(t)\right\rangle &= \int_0^t \mathbb{E}\left\langle \ddot{U}_g^2(\tau)\right\rangle \mathrm{d}\tau = \int_0^t \sigma_{\ddot{U}g}^2(\tau)\,\mathrm{d}\tau \\ &= \int_0^t A^2(\tau)\,\mathrm{d}\tau\end{aligned} \tag{B.2}$$

A least-square fitting can be used to calibrate the sought amplitude $A(t)$ [57].

An alternative approach is proposed here, based on the following assumption:

$$I_f(t) = \mathbb{E}\left\langle I_{\ddot{U}g}(t)\right\rangle\,, \tag{B.3}$$

i.e., that the deterministic function $I_f(t)$ coincides with the mean value of the cumulative intensity function of the piecewise uniformly modulated random process $I_{\ddot{U}g}(t)$, fully defined by Eq. (7).

Substituting Eq. (B.2) into Eq. (B.3) and differentiating both sides with respect to the time t, one obtains an explicit relationship between the modulating function $A(t)$ and the intensity of the cumulative intensity function of the parent signal:

$$A(t) = \sqrt{\frac{\mathrm{d}}{\mathrm{d}t}\,I_f(t)}\,. \tag{B.4}$$

In practical applications, the (continuous-time) derivative under the square root in the right-hand side of Eq. (B.4) can be replaced with the (discrete-time) difference quotient, i.e., the average rate of change of $I_f(t)$ over a smoothing time interval of center $t_\ell = \ell\,\Delta t$ and width $\hat{\Delta t} = 2\,p\,\Delta t$, where $p \ge 1$ is the integer representing the number of time steps Δt in half of the discrete-time width $\hat{\Delta t}$. This approximation leads to:

$$A_\ell = A(t_\ell) = \sqrt{\frac{I_f\left(t_\ell + \hat{\Delta t}/2\right) - I_f\left(t_\ell - \hat{\Delta t}/2\right)}{\hat{\Delta t}}}\,, \tag{B.5}$$

where a linear interpolation can be assumed between the amplitudes values A_ℓ and $A_{\ell+1}$ at two consecutive discrete times t_ℓ and $t_{\ell+1} = t_\ell + \Delta t$. To avoid inconsistent results, the conditions $A(0) = 0$ must be satisfied.

References

[1] A.K. Chopra, Dynamics of Structures in SI Units, Pearson, Harlow, U.K., 2020.
[2] P. Fajfar, Analysis in seismic provisions for buildings: Past, present and future, in: K. Pitilakis (Ed.), Recent Advances in Earthquake Engineering in Europe, Vol. 46, Springer, Cham, Switzerland, 2018, pp. 1–49.
[3] G. Muscolino, F. Genovese, A. Sofi, Reliability bounds for structural systems subjected to a set of recorded accelerograms leading to imprecise seismic power spectrum, ASCE-ASME J. Risk Uncertain. Eng. Syst. A 8 (2) (2022) 04022009.
[4] E.I. Katsanos, A.G. Sextos, G.D. Manolis, Selection of earthquake ground motion records: A state-of-the-art review from a structural engineering perspective, Soil Dyn. Earthq. Eng. 30 (4) (2010) 157–169.
[5] E.H. Vanmarcke, State-of-the-Art for Assessing Earthquake Hazards in the United States. Report 14. Representation of Earthquake Ground Motion: Scaled Accelerograms and Equivalent Response Spectra, Technical Report 14, Department of Civil Engineering, Massachusetts Institute of Technology, Cambridge, Massachusetts, 1979.
[6] J.J. Bommer, B. Acevedo, The use of real earthquake accelerograms as input to dynamic analysis, J. Earthq. Eng. 8 (Special Issue 1) (2004) 43–91.
[7] E. Cavdar, G. Ozdemir, B. Bayhan, Significance of ground motion scaling parameters on amplitude of scale factors and seismic response of short- and long-period structures, Earthq. Spectra 35 (4) (2019) 1663–1688.
[8] H. Dávalos, E. Miranda, Evaluation of the scaling factor bias influence on the probability of collapse using $S_a(T_1)$ as the intensity measure, Earthq. Spectra 35 (2) (2019) 679–702.
[9] F. Genovese, Influence of soil non-linear behaviour on the selection of input motion for dynamic geotechnical analysis, in: M. Barla, A. Di Donna, D. Sterpi (Eds.), Challenges and Innovations in Geomechanics, Vol. 126, Springer, Cham, Switzerland, 2021, pp. 588–596.

[10] Y.G. Li, H.P. Hong, Use of spectrum-matched versus scaled records to evaluate seismic responses of a latticed shell, J. Earthq. Eng. 26 (8) (2022) 4054–4068.
[11] J.E. Carballo, C.A. Cornell, Probabilistic seismic demand analysis: Spectrum matching and design, Technical Report RMS-41, Department of Civil and Environmental Engineering, Stanford University, Stanford, California, 2000, p. 313.
[12] E.H. Vanmarcke, D.A. Gasperini, Simulated earthquake ground motions, in: International Conference on Structural Mechanics in Reactor Technology, San Francisco, California, 1977, p. K1/9.
[13] M.K. Kaul, Stochastic characterization of earthquakes through their response spectrum, Earthq. Eng. Struct. Dyn. 6 (5) (1978) 497–509.
[14] C. Sundararajan, An iterative method for the generation of seismic power spectral density functions, Nucl. Eng. Des. 61 (1) (1980) 13–23.
[15] A. Preumont, A method for the generation of artificial earthquake accelerograms, Nucl. Eng. Des. 59 (2) (1980) 357–368.
[16] D.D. Pfaffinger, Calculation of power spectra from response spectra, J. Eng. Mech. 109 (1) (1983) 357–372.
[17] A. Preumont, The generation of spectrum compatible accelerograms for the design of nuclear power plants, Earthq. Eng. Struct. Dyn. 12 (4) (1984) 481–497.
[18] P. Cacciola, P. Colajanni, G. Muscolino, Combination of modal responses consistent with seismic input representation, J. Struct. Eng. 130 (1) (2004) 47–55.
[19] K.A. Bani-Hani, A.I. Malkawi, A multi-step approach to generate response-spectrum-compatible artificial earthquake accelerograms, Soil Dyn. Earthq. Eng. 97 (2017) 117–132.
[20] G. Barone, F. Lo Iacono, G. Navarra, A. Palmeri, A novel analytical model of power spectral density function coherent with earthquake response spectra, in: Proceedings of the 1st International Conference on Uncertainty Quantification in Computational Sciences and Engineering (UNCECOMP 2015), Institute of Structural Analysis and Antiseismic Research School of Civil Engineering National Technical University of Athens (NTUA) Greece, Crete Island, Greece, 2015, pp. 394–406, http://dx.doi.org/10.7712/120215.4280.805, URL http://www.eccomasproceedia.org/conferences/thematic-conferences/uncecomp-2015/4280.
[21] G. Barone, F. Lo Iacono, G. Navarra, A. Palmeri, Closed-form stochastic response of linear building structures to spectrum-consistent seismic excitations, Soil Dyn. Earthq. Eng. 125 (2019) 105724.
[22] G. Rodolfo Saragoni, G.C. Hart, Simulation of artificial earthquakes, Earthq. Eng. Struct. Dyn. 2 (3) (1973) 249–267.
[23] A. Der Kiureghian, J. Crempien, An evolutionary model for earthquake ground motion, Struct. Saf. 6 (2–4) (1989) 235–246.
[24] S. Rezaeian, A. Der Kiureghian, A stochastic ground motion model with separable temporal and spectral nonstationarities, Earthq. Eng. Struct. Dyn. 37 (13) (2008) 1565–1584.
[25] J.-J. Wang, J. Zhou, Aseismic designs based on artificial simulations, IEEE Signal Process. Mag. 16 (2) (1999) 94–99.
[26] C. Kafali, M. Grigoriu, Seismic fragility analysis: Application to simple linear and nonlinear systems, Earthq. Eng. Struct. Dyn. 36 (13) (2007) 1885–1900.
[27] M. Grigoriu, To scale or not to scale seismic ground-acceleration records, J. Eng. Mech. 137 (4) (2011) 284–293.
[28] C. Vetter, A.A. Taflanidis, Comparison of alternative stochastic ground motion models for seismic risk characterization, Soil Dyn. Earthq. Eng. 58 (2014) 48–65.
[29] P. Naga, M.R. Eatherton, Analyzing the effect of moving resonance on seismic response of structures using wavelet transforms, Earthq. Eng. Struct. Dyn. 43 (5) (2014) 759–768.
[30] Y. Li, J.P. Conte, M. Barbato, Influence of time-varying frequency content in earthquake ground motions on seismic response of linear elastic systems, Earthq. Eng. Struct. Dyn. 45 (8) (2016) 1271–1291.
[31] D. Tao, J. Lin, Z. Lu, Time-frequency energy distribution of ground motion and its effect on the dynamic response of nonlinear structures, Sustainability 11 (3) (2019) 702.
[32] A. Marin, P.L. Truffer, I. Anastasopoulos, Combined-intensity-measures matching approach for improved performance-based design of slopes, Soil Dyn. Earthq. Eng. 126 (2019) 105763.
[33] A. Der Kiureghian, K. Fujimura, Nonlinear stochastic dynamic analysis for performance-based earthquake engineering, Earthq. Eng. Struct. Dyn. 38 (5) (2009) 719–738.
[34] A. Palmeri, F. Ricciardelli, G. Muscolino, A. De Luca, Random vibration of systems with viscoelastic memory, J. Eng. Mech. 130 (9) (2004) 1052–1061.
[35] D. De Domenico, G. Ricciardi, Earthquake protection of structures with nonlinear viscous dampers optimized through an energy-based stochastic approach, Eng. Struct. 179 (2019) 523–539.
[36] M. Argenziano, E. Mele, A. Palmeri, Optimal design of viscoelastic tuned mass dampers for structures exposed to coloured excitations, in: Current Perspectives and New Directions in Mechanics, Modelling and Design of Structural Systems, CRC Press, 2022, Num Pages: 7.
[37] A. Preumont, The generation of non-separable artificial earthquake accelerograms for the design of nuclear power plants, Nucl. Eng. Des. 88 (1) (1985) 59–67.
[38] P. Cacciola, A stochastic approach for generating spectrum compatible fully nonstationary earthquakes, Comput. Struct. 88 (15–16) (2010) 889–901.
[39] P. Cacciola, I. Zentner, Generation of response-spectrum-compatible artificial earthquake accelerograms with random joint time–frequency distributions, Probab. Eng. Mech. 28 (2012) 52–58.
[40] P. Cacciola, L. D'Amico, I. Zentner, New insights in the analysis of the structural response to response-spectrum-compatible accelerograms, Eng. Struct. 78 (2014) 3–16.
[41] S. Mukherjee, V.K. Gupta, Wavelet-based generation of spectrum-compatible time-histories, Soil Dyn. Earthq. Eng. 22 (9–12) (2002) 799–804.
[42] D. Cecini, A. Palmeri, Spectrum-compatible accelerograms with harmonic wavelets, Comput. Struct. 147 (2015) 26–35.
[43] S. Mukhopadhyay, S. Das, V.K. Gupta, Wavelet-based generation of accelerogram-consistent, spectrum-compatible motions: New algorithms and short-period overestimation, Soil Dyn. Earthq. Eng. 121 (2019) 327–340.
[44] P. Spanos, L. Vargas Loli, A statistical approach to generation of design spectrum compatible earthquake time histories, Int. J. Soil Dyn. Earthq. Eng. 4 (1) (1985) 2–8.
[45] P.D. Spanos, A. Giaralis, J. Li, Synthesis of accelerograms compatible with the Chinese GB 50011-2001 design spectrum via harmonic wavelets: Artificial and historic records, Earthq. Eng. Eng. Vibr. 8 (2) (2009) 189–206.
[46] A. Giaralis, P.D. Spanos, Derivation of response spectrum compatible non-stationary stochastic processes relying on Monte Carlo-based peak factor estimation, Earthq. Struct. 3 (3_4) (2012) 581–609.
[47] A. Giaralis, P. Spanos, Wavelet-based response spectrum compatible synthesis of accelerograms - Eurocode application (EC8), Soil Dyn. Earthq. Eng. 29 (1) (2009) 219–235.
[48] C.-H. Yeh, Y. Wen, Modeling of nonstationary ground motion and analysis of inelastic structural response, Struct. Saf. 8 (1–4) (1990) 281–298.
[49] J. Beck, C. Papadimitriou, Moving resonance in nonlinear response to fully nonstationary stochastic ground motion, Probab. Eng. Mech. 8 (3–4) (1993) 157–167.
[50] J. Wang, L. Fan, S. Qian, J. Zhou, Simulations of non-stationary frequency content and its importance to seismic assessment of structures, Earthq. Eng. Struct. Dyn. 31 (4) (2002) 993–1005.
[51] H. Cao, M. Friswell, The effect of energy concentration of earthquake ground motions on the nonlinear response of RC structures, Soil Dyn. Earthq. Eng. 29 (2) (2009) 292–299.
[52] H. Aknouche, A. Airouche, H. Bechtoula, Influence of earthquake frequency nonstationarity on seismic structural response, Iran. J. Sci. Technol., Trans. Civ. Eng. 44 (2) (2020) 603–614.
[53] M. Shinozuka, Y. Sato, Simulation of nonstationary random process, J. Eng. Mech. Div. 93 (1) (1967) 11–40.
[54] M. Shinozuka, Monte Carlo solution of structural dynamics, Comput. Struct. 2 (5–6) (1972) 855–874.
[55] M. Shinozuka, C.-M. Jan, Digital simulation of random processes and its applications, J. Sound Vib. 25 (1) (1972) 111–128.
[56] D. Cecini, A. Palmeri, Spectrum-Compliant Accelerograms Through Harmonic Wavelet Transform, Dubrovnik, Croatia, 2012, p. Paper 285, http://dx.doi.org/10.4203/ccp.99.285, URL http://www.ctresources.info/ccp/paper.html?id=7127.
[57] G. Muscolino, F. Genovese, G. Biondi, E. Cascone, Generation of fully non-stationary random processes consistent with target seismic accelerograms, Soil Dyn. Earthq. Eng. 141 (2021) 106467.
[58] D.K. Kwon, A. Kareem, Other Models: Data-Driven Approaches for Non-Stationary Non-Synoptic Winds, in: H. Hangan, A. Kareem (Eds.), The Oxford Handbook of Non-Synoptic Wind Storms, Oxford University Press, 2021, http://dx.doi.org/10.1093/oxfordhb/9780190670252.013.24.
[59] L. Roncallo, G. Solari, G. Muscolino, F. Tubino, Maximum dynamic response of linear elastic SDOF systems based on an evolutionary spectral model for thunderstorm outflows, J. Wind Eng. Ind. Aerodyn. 224 (2022) 104978, http://dx.doi.org/10.1016/j.jweia.2022.104978.
[60] J.J. Bommer, Earthquake hazard and risk analysis for natural and induced seismicity: towards objective assessments in the face of uncertainty, Bull. Earthq. Eng. 20 (6) (2022) 2825–3069, http://dx.doi.org/10.1007/s10518-022-01357-4.
[61] C.J. Keylock, Hypothesis testing for nonlinear phenomena in the geosciences using synthetic, surrogate data, Earth Space Sci. (2018) http://dx.doi.org/10.1029/2018EA000435, 2018EA000435.
[62] M.O. Khan, K. Valen-Sendstad, D.A. Steinman, Direct numerical simulation of laminar-turbulent transition in a non-axisymmetric stenosis model for Newtonian vs. shear-thinning non-Newtonian rheologies, Flow Turbul. Combust. 102 (1) (2019) 43–72, http://dx.doi.org/10.1007/s10494-018-9905-7.
[63] V. Laface, I.A. Kougioumtzoglou, G. Malara, F. Arena, Efficient processing of water wave records via compressive sensing and joint time-frequency analysis via harmonic wavelets, Appl. Ocean Res. 69 (2017) 1–9, http://dx.doi.org/10.1016/j.apor.2017.09.011.
[64] Y. Zhou, X. Hang, S. Wu, Q. Fei, N. Trisovic, Frequency-dependent random fatigue of panel-type structures made of ceramic matrix composites, Acta Mech. Solida Sin. 30 (2) (2017) 165–173, http://dx.doi.org/10.1016/j.camss.2017.03.010.
[65] K. Kwon, D.M. Frangopol, Bridge fatigue reliability assessment using probability density functions of equivalent stress range based on field monitoring data, Int. J. Fatigue 32 (8) (2010) 1221–1232, http://dx.doi.org/10.1016/j.ijfatigue.2010.01.002.

[66] M. Lancieri, P. Bazzurro, O. Scotti, Spectral matching in time domain: A seismological and engineering analysis, Bull. Seismol. Soc. Am. 108 (4) (2018) 1972–1994, http://dx.doi.org/10.1785/0120170396.
[67] S. Mallat, A Wavelet Tour of Signal Processing: The Sparse Way, third ed., Elsevier, Amsterdam, 2009.
[68] D.E. Newland, Harmonic wavelet analysis, Proc. R. Soc. Lond. Ser. A Math. Phys. Eng. Sci. 443 (1917) (1993) 203–225, http://dx.doi.org/10.1098/rspa.1993.0140.
[69] D.E. Newland, Harmonic and musical wavelets, Proc. R. Soc. Lond. Ser. A Math. Phys. Eng. Sci. 444 (1922) (1994) 605–620, http://dx.doi.org/10.1098/rspa.1994.0042.
[70] D.E. Newland, Wavelet analysis of vibration: Part 1 - Theory, J. Vib. Acoust. 116 (4) (1994) 409–416, http://dx.doi.org/10.1115/1.2930443.
[71] D.E. Newland, Wavelet analysis of vibration: Part 2 - Wavelet maps, J. Vib. Acoust. 116 (4) (1994) 417–425, http://dx.doi.org/10.1115/1.2930444.
[72] C. Jacob, K. Sepahvand, V.A. Matsagar, S. Marburg, Stochastic seismic response of base-isolated buildings, Int. J. Appl. Mech. 05 (01) (2013) 1350006, http://dx.doi.org/10.1142/S1758825113500063.
[73] B. Basu, V.K. Gupta, Wavelet-based non-stationary response analysis of a friction base-isolated structure, Earthq. Eng. Struct. Dyn. 29 (11) (2000) 1659–1676, http://dx.doi.org/10.1002/1096-9845(200011)29:11<1659::AID-EQE983>3.0.CO;2-S.
[74] S.K. Saha, V.A. Matsagar, A.K. Jain, Seismic fragility of base-isolated water storage tanks under non-stationary earthquakes, Bull. Earthq. Eng. 14 (4) (2016) 1153–1175, http://dx.doi.org/10.1007/s10518-016-9874-y.
[75] A. Ali, N. Abu-Hayah, D. Kim, S.G. Cho, Design response spectra-compliant real and synthetic GMS for seismic analysis of seismically isolated nuclear reactor containment building, Nucl. Eng. Technol. 49 (4) (2017) 825–837, http://dx.doi.org/10.1016/j.net.2017.02.006.
[76] J. Liang, S.R. Chaudhuri, M. Shinozuka, Simulation of nonstationary stochastic processes by spectral representation, J. Eng. Mech. 133 (6) (2007) 616–627, http://dx.doi.org/10.1061/(ASCE)0733-9399(2007)133:6(616).
[77] J.P. Conte, B.F. Peng, Fully nonstationary analytical earthquake ground-motion model, J. Eng. Mech. 123 (1) (1997) 15–24, http://dx.doi.org/10.1061/(ASCE)0733-9399(1997)123:1(15).
[78] M.B. Priestley, Evolutionary spectra and non-stationary processes, J. R. Stat. Soc. Ser. B Stat. Methodol. 27 (2) (1965) 204–229, http://dx.doi.org/10.1111/j.2517-6161.1965.tb01488.x.
[79] M.D. Trifunac, Zero baseline correction of strong-motion accelerograms, Bull. Seismol. Soc. Am. 61 (5) (1971) 1201–1211, http://dx.doi.org/10.1785/BSSA0610051201.
[80] M.D. Trifunac, F.E. Udwadia, A.G. Brady, Analysis of errors in digitized strong-motion accelerograms, Bull. Seismol. Soc. Am. 63 (1) (1973) 157–187, http://dx.doi.org/10.1785/BSSA0630010157.
[81] D.M. Boore, Effect of baseline corrections on displacements and response spectra for several recordings of the 1999 Chi-Chi, Taiwan, earthquake, Bull. Seismol. Soc. Am. 91 (5) (2004) 1199–1211, http://dx.doi.org/10.1785/0120000703.
[82] D.M. Boore, J.J. Bommer, Processing of strong-motion accelerograms: Needs, options and consequences, Soil Dyn. Earthq. Eng. 25 (2) (2005) 93–115, http://dx.doi.org/10.1016/j.soildyn.2004.10.007.
[83] J.J. Bommer, P.J. Stafford, Estimating ground motion levels in earthquake damage investigations: a framework for forensic engineering seismology, Int. J. Forensic Eng. 1 (1) (2012) 3, http://dx.doi.org/10.1504/IJFE.2012.047444.
[84] N. Ntritsos, M. Cubrinovski, B.A. Bradley, Challenges in the definition of input motions for forensic ground-response analysis in the near-source region, Earthq. Spectra 37 (4) (2021) 2562–2595, http://dx.doi.org/10.1177/87552930211001376.
[85] E.L. Krinitzsky, How to obtain earthquake ground motions for engineering design, Eng. Geol. (2002) 16.
[86] T. Lin, C.B. Haselton, J.W. Baker, Conditional spectrum-based ground motion selection. Part I: Hazard consistency for risk-based assessments, Earthq. Eng. Struct. Dyn. 42 (12) (2013) 1847–1865, http://dx.doi.org/10.1002/eqe.2301.
[87] T. Lin, C.B. Haselton, J.W. Baker, Conditional spectrum-based ground motion selection. Part II: Intensity-based assessments and evaluation of alternative target spectra, Earthq. Eng. Struct. Dyn. 42 (12) (2013) 1867–1884, http://dx.doi.org/10.1002/eqe.2303.
[88] I. Zentner, A procedure for simulating synthetic accelerograms compatible with correlated and conditional probabilistic response spectra, Soil Dyn. Earthq. Eng. 63 (2014) 226–233, http://dx.doi.org/10.1016/j.soildyn.2014.03.012.
[89] B.Ö. Ay, M.J. Fox, T.J. Sullivan, Technical note: Practical challenges facing the selection of conditional spectrum-compatible accelerograms, J. Earthq. Eng. 21 (1) (2017) 169–180, http://dx.doi.org/10.1080/13632469.2016.1157527.
[90] M. Kohrangi, P. Bazzurro, D. Vamvatsikos, A. Spillatura, Conditional spectrum-based ground motion record selection using average spectral acceleration, Earthq. Eng. Struct. Dyn. 46 (10) (2017) 1667–1685, http://dx.doi.org/10.1002/eqe.2876.
[91] P.J. Stafford, Interfrequency correlations among Fourier spectral ordinates and implications for stochastic ground-motion simulation, Bull. Seismol. Soc. Am. 107 (6) (2017) 2774–2791, http://dx.doi.org/10.1785/0120170081.
[92] K. Trevlopoulos, I. Zentner, Seismic fragility curve assessment based on synthetic ground motions with conditional spectra, Pure Appl. Geophys. 177 (5) (2020) 2375–2390, http://dx.doi.org/10.1007/s00024-019-02245-w.
[93] T.D. Ancheta, R.B. Darragh, J.P. Stewart, E. Seyhan, W.J. Silva, B.S.-J. Chiou, K.E. Wooddell, R.W. Graves, A.R. Kottke, D.M. Boore, T. Kishida, J.L. Donahue, NGA-West2 Database, Earthq. Spectra 30 (3) (2014) 989–1005, http://dx.doi.org/10.1193/070913EQS197M.